이학석사학위논문

Development of Atmospheric Correction Algorithm for Geostationary Ocean Color Imager (GOCI)

정지궤도해색위성(GOCI)를 위한 대기보정 기술의 개발

2012년 8월

서울대학교 대학원

지구환경과학부

안 재 현

Development of Atmospheric Correction Algorithm for Geostationary Ocean Color Imager (GOCI)

Jae Hyun Ahn

School of Earth and Environmental Sciences

Seoul National University

June 2012

Development of Atmospheric Correction Algorithm
for Geostationary Ocean Color Imager (GOCI)

지도교수 오 임 상

이 논문을 이학석사 학위논문으로 제출함

2012년 4월

서울대학교 대학원
지구환경과학부
안 재 현

안재현의 이학석사 학위논문을 인준함

2012년 6월

위 원 장 _____ (인)

부위원장 _____ (인)

위 원 _____ (인)

Abstract

This thesis describes an atmospheric correction algorithm of Geostationary Ocean Color Imager (GOCI) which is to be implemented in GOCI Data Processing System (GDPS) – developed by the Korea Ocean Satellite Center of the Korea Ocean Research and Development Institute. The algorithm is based on the standard atmospheric algorithm of the Sea-viewing Wide Field-of-view Sensor (SeaWiFS) data which accounts for multiple scattering effects; and is partially updated in terms of turbid case-2 water correction, aerosol models and slot correction. For turbid water correction, we used a regional empirical relationship between normalized water reflectance at the red and near infrared bands. The relationship was derived from normalized water-leaving reflectances in turbid pixels in satellite images after atmospheric correction that processed using aerosol properties (such as aerosol optical thickness and aerosol type) derived from nearest neighboring non-turbid waters. This satellite derived data based empirical model showed a less scattered relationship than the *in situ* measurements. In order to validate the GOCI atmospheric correction, we compared our results with *in situ* measurements of normalized water leaving radiance (nLw) spectra, which had been obtained during several cruises in 2011 around in the Korean seas. The validation results are encouraging especially for turbid waters. The validation in clear waters implies that the atmospheric correction should be improved in the future. Vicarious calibration would improve the results for the

clear waters, although a part of the deviation arose from uncertainties in the above water nLw measurements.

Keyword : GOCI, atmospheric correction, ocean color, case-2 water, near infrared correction

Table of Contents

List of Figures

List of Tables

1. Introduction

1.1 Atmospheric correction

Ocean color remote sensing

Satellite remote sensing of ocean color is a work with imagery from satellite radiometers observing the ocean in the visible and near infrared (NIR) wavelengths. There are a lot of applications such as monitoring chlorophyll concentration, detecting short term biophysical phenomena, studies on biogeochemical variables and cycle, detecting noxious or toxic algal blooms of notable extension, monitoring the health of marine ecosystem, coastal zone and resource management, producing an improved marine fisheries information to the fisherman communities, deriving Yellow dust and the land classified information and monitoring the primary production (Fig. 1.). Hence, ocean color remote sensing has become one of the most important methods to observe the ocean environment system. Since the first ocean color satellite, Coastal Zone Color Scanner (CZCS), launched in 1978, satellite remote sensing data can be acquired from large area and fast access, so the ocean color remote sensing research has developed rapidly.

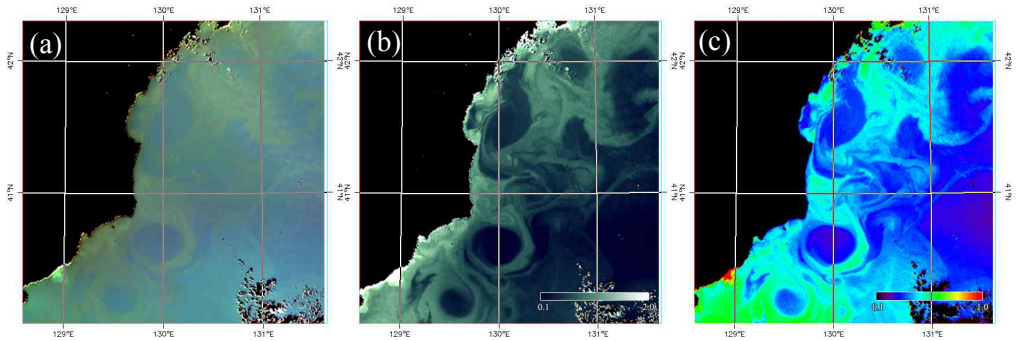

Fig. 1. Ocean colour remote sensing products, (a) is water-leaving radiance (b) is chlorophyll concentration (c) is total suspended sediment

Geostationary Ocean Color Imager (GOCI)

The world first Geostationary Ocean Color Imager (GOCI) is one of the three payloads of the Communication-Ocean-Meteorological Satellite (COMS) (Fig. 2.) and designed to the

latest specification (Table 1.). Unlike previous sensors loaded in the polar orbit satellites to observe the target area only once per a day, GOCI acquires 8 daytime images per a day from local time 09:15 to 16:15. It observes over Korean seas (Fig 3.) in 8 spectral bands (6 visible, 2 NIR) based on spectral requirements for GOCI's mission (Table 2.) and a spatial resolution is about 500 m. The satellite ocean color remote sensing products mainly include the chlorophyll-a concentration, optical diffuse attenuation coefficients, concentration of dissolved organic material or yellow substance, and the concentration of suspended particles in the near-surface zone of the sea. In operational oceanography, the satellite-derived products are used in conjunction with numerical models and *in situ* measurements to provide forecasting and now casting of the ocean state.

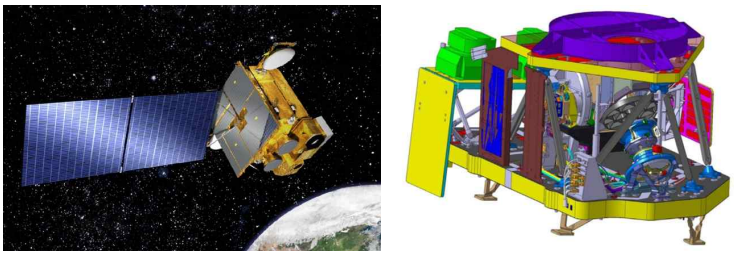

Fig. 2. COMS satellite (left) and GOCI payload (right)

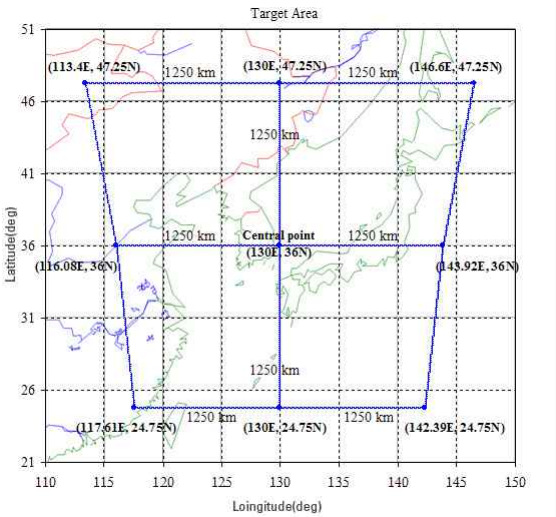

Fig. 3. GOCI's observation area

Description	Specification
Detector	CMOS (2D, 1415×1432 pixels)
Image capture (sequence)	2D Staring frame capture Dark Signal → High gain → Low gain → Dark Signal
Radiometric Calibration	Solar diffuser & DAMD(Diffuser Aging Monitoring Device)
Resolution (GSD)	500m×500m
Total FOV	16 slots, 5,300×5,300 Pixels
Coverage	2,500km×2,500km
Longitude	128.2˚E
Altitude	35,786km
Pupil Diameter of Pointing Mirror	140mm
SNR	> 1,000
MTF	> 0.3
Number of Spectral Bands	8 Bands (6-Visible and 2-NIR)
Digitization	≥ 12 bits

Table 1. Specification of GOCI

Band	Center wavelength	Band width	SNR	Type	Primary application
B1	412nm	20nm	1077	Visible	Yellow substance and turbidity
B2	443nm	20nm	1199	Visible	Chlorophyll absorption maximum
B3	490nm	20nm	1316	Visible	Chlorophyll and other pigments
B4	555nm	20nm	1223	Visible	Turbidity, suspended sediment
B5	660nm	20nm	1192	Visible	Baseline of fluorescence signal, Chlorophyll, suspended sediment
B6	680nm	10nm	1093	Visible	Atmospheric correction and fluorescence signal
B7	745nm	20nm	1107	NIR	Atmospheric correction and baseline of fluorescence signal
B8	865nm	40nm	1009	NIR	Aerosol optical thickness, vegetation, water vapor reference over the ocean

Table 2. Spectral requirements for GOCI's mission

Atmospheric correction

GOCI measures the spectral distribution of radiance from the top-of-atmosphere (TOA) like all other ocean color satellite. For better ocean color data such as chlorophyll, suspended sediment, colored organic matter and etc., it is indispensable to have we require the accurate spectral distribution of radiance or reflectance upwelling from below the ocean surface as Fig. 4. To estimate more accurate radiance emerging from the ocean, the scattering radiances from the atmosphere (e.g., molecular and aerosol) and surface contributions (e.g., specular reflection and white-caps) must be accurately retrieved from satellite-measured radiances by atmospheric correction process.

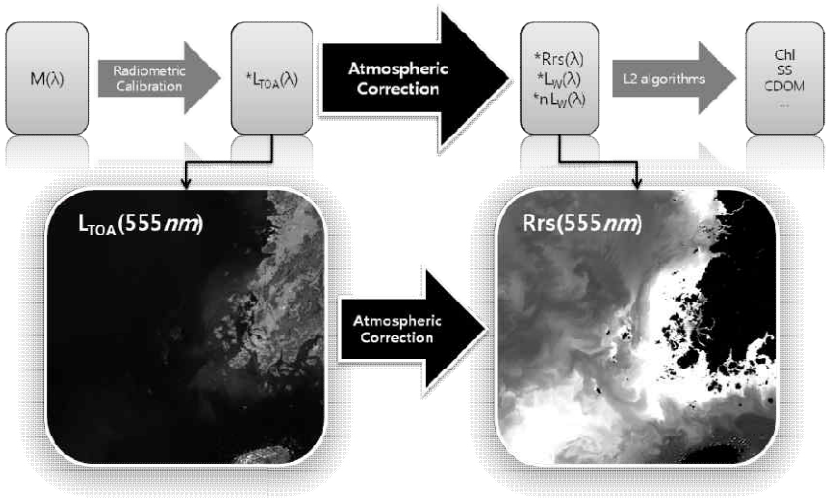

Fig. 4. Diagram of ocean color data processing and some example images

Atmospheric correction is a very sophisticated and important process, because these atmospheric radiances can occupy over 90% of the total satellite-measured radiances. Thus, the atmospheric correction results are sensitive, i.e. 1% error in the atmospheric correction could cause more than 10% error in the ocean radiance estimation (Fig. 5.). In the case of the Geostationary Ocean Color Imager (GOCI), the mean cosine value of the satellite zenith angle is 0.75. Thus, the GOCI has a longer optical path than other polar orbit sensors such as the Moderate-Resolution Imaging Spectroradiometer (MODIS) is 0.85 or the Medium-Resolution Imaging Spectrometer (MERIS) is 0.94 (Fig. 6.).

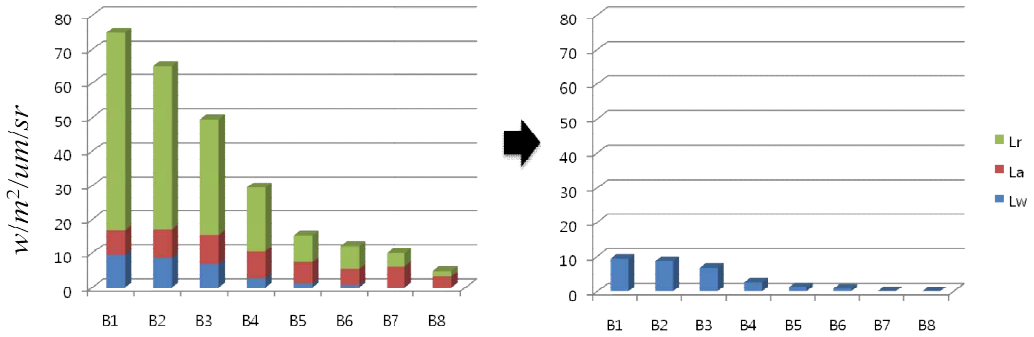

Fig. 5. A comparison between atmosphere and pure ocean signal (L_r is the radiance from molecular scattering, L_a is the radiance from aerosol scattering, L_w is the radiance from the ocean)

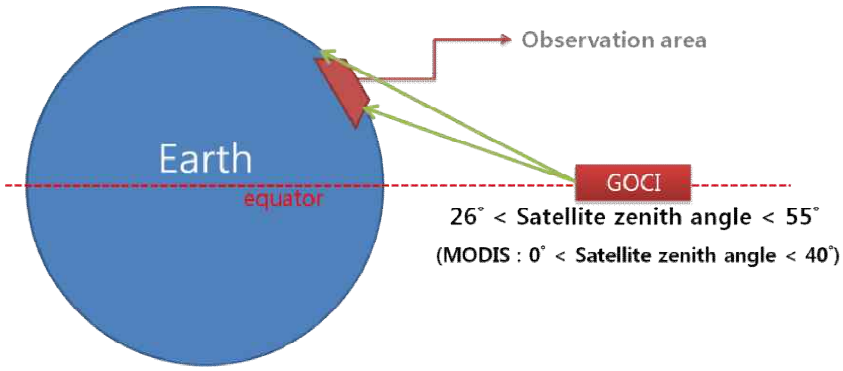

Fig. 6. Extended optical thickness of geostationary orbit satellite

Earlier atmospheric correction algorithms for the ocean color remote sensing assumed that the ocean radiance is negligible at the near-infrared (NIR) spectral range, so that only atmospheric radiance remains in these bands, so called as black pixel assumption (Gordon, 1978). The atmospheric correction algorithm with black pixel assumption is first developed for CZCS data by Gordon (1978, 1983). This algorithm is based on the single scattering approximation for atmospheric particles. For low aerosol optical thickness (AOT) cases, this single-scattering-based estimation is generally reasonable. For more

general cases and better accuracy, more advanced atmospheric correction method such contains a multiple scattering consideration and per-pixel aerosol model selection was developed and applied for the SeaWiFS data (Gordon and Wang, 1994). However, for extremely turbid coastal waters, the ocean radiance can be significant even at NIR wavelengths. This means that the black pixel assumption is no longer valid. We note that a number of studies addressed the atmospheric correction for turbid waters (Hu et al., 2000; Ruddick et al., 2000; Siegel et al., 2000; Wang et al., 2007, 2009, 2011). The GOCI coverage contains highly turbid water areas such as the Yellow Sea, the East China Sea, and the coastal areas of the Korean peninsula. In this respect, the implementation of turbid atmospheric correction in the GOCI Data processing chains is of a high priority. A focus of this study is on a new case-2 water (i.e., inorganic particles are dominant) improvement for GOCI's observation area. We found a strong relationship between satellite-derived ocean reflectances at red and NIR bands in the turbid coastal waters. To correct the atmospheric effects accurately for case-2 waters, we used an iterative method with the empirical relationship.

In section 2, we summarize the present atmospheric correction method for the ocean color remote sensing, which is followed by description of the modified and optimized features for the GOCI data processing: a different acquisition time per slot for atmospheric correction and applied aerosol models. Section 3 describes results of validation with *in situ* nLw data. In Section 4, we presented discussions and conclusions.

This atmospheric correction algorithm will be included in the next version of the GOCI Data Processing System (GDPS) and is expected to improve the reliability of the GOCI level 2 products.

1.2 Previous studies

The systematic measurements of the ocean spectra from aircraft were first conducted by Clarke et al.(1970). The spectral measurements of the light backscattered from the sea from altitudes ranging about from 0.15 to 3.0 *km* showed the effect of increasing *air light* on the upward radiance received by the sensor. Thus, this is the first approach of the 'atmospheric correction' (Austin, 1974; Clarke and Ewing, 1974). The study of removing the atmospheric and surface effects from satellite imagery of the ocean was examined (Gordon, 1978; Gordon and Clark, 1980; Morel, 1980), and the technique developed for that purpose (Gordon, 1980) was then implemented into the NASA processing system used with the NIMBUS-7 Coastal Zone Color Scanner (CZCS) sensor.

The CZCS algorithm

Removal of atmospheric effects for the ocean color remote sensing was firstly developed for CZCS data by Gordon (1978). This algorithm relies on the basis of some assumption (i) water-leaving radiance of NIR wavelength (670*nm*) is negligible and total signal of NIR bands are only from the atmospheric scattering (i.e., black pixel assumption), (ii) the aerosol scattering phase function should be nearly independent of wavelength, and (iii) all photons are scattered only once by atmospheric particles (i.e., single scattering approximation). However, this single scattering approximation is no more acceptable when the optical thickness of atmosphere (τ) is over 0.2.

The SeaWiFS/MODIS algorithm

The multiple scattering and coupling of the aerosol molecular scattering were first addressed by Gordon and Wang (1994a) for SeaWiFS data, and are currently adopted for a standard atmospheric correction of NASA ocean color remote sensing data. It selects an aerosol type of 12 aerosol models by the slope of two NIR (765*nm*, 865*nm*) reflectances, and process the atmospheric correction with visible band expanded reflectances by a specific aerosol type, a geometric angle and an aerosol optical thickness. The schemes for

this atmospheric correction, such as those presented in this report, include multiple scattering consideration and selection of various types of aerosols.

The OCTS/GLI algorithm

The atmospheric correction algorithm for the Ocean Color and Temperature Sensor (OCTS) and the Global Imager (GLI) data is based on the SeaWiFS atmospheric correction method, although the implementation of algorithm has some differences (Fukushima et al., 1998). In contrast to the atmospheric correction algorithm of SeaWiFS and MODIS data, it adopts a set of 10 aerosol models (SeaWiFS/MODIS algorithm has 12 aerosol models) and uses relationship between aerosol's multiple scattering and optical thickness (SeaWiFS/MODIS algorithm uses relationship between multiple scattering and single scattering).

The MERIS algorithm

The scheme of the standard atmospheric correction algorithm for the MERIS is first described and tested by Antoine and Morel (1998, 1999). Similar to the NASA standard atmospheric correction, this method also adopted the black pixel assumption and multiple scattering consideration. The main difference between MERIS and SeaWiFS/MODIS atmospheric correction algorithm is removal of the total atmospheric path signal at once, instead of separate assessments Rayleigh and aerosol signals. It selects aerosol models with two NIR reflectances of total path signal by the iterative method.

The SSMM algorithm

The spectral shape matching method(SSMM) is the GOCI's first atmospheric correction algorithm that uses a normalized spectral shape of the reference site (Shanmugam and Ahn, 2007). SSMM sets a reference target where the spectrum shape does not change such as extremely turbid water or oligotrophic open oceans, and the oceanographic observation tower that provides in-situ spectra also can be a reference site. SSMM selects an aerosol type from several reference sites and perform atmospheric correction over

clear and turbid waters based on a assumption that the selected aerosol type is horizontally homogeneous.

The POLYMER algorithm

The polynomial-based algorithm applied to MERIS (POLYMER) data is a simple spectral matching method (Steinmetz, 2011) that can be computed by iteration method (or neural network) between ocean color model (Morel and Maritorena, 2001) and a simple a quartic polynomial atmospheric model. This also processes a robust sun glint correction during Rayleigh scattering correction. Polymer is originally developed to process MERIS data, but is currently support to process multiple sensors such as; MODIS and GOCI (Sun Glint Correction Algorithm; SGCA). The SCGA will be optionally included by the future version of GDPS.

2. SeaWiFS atmospheric correction algorithm and its extension for GOCI

The standard atmospheric correction algorithm for GOCI data is also theoretically based on the SeaWiFS/MODIS algorithm. In this section, a review of the prevalent atmospheric correction algorithm, that is based on the SeaWiFS atmospheric correction algorithm, such considers the atmosphere's multiple scattering effects and the updated features: the case-2 water correction, the aerosol model used, and the slot corrections.

2.1. A Classical atmospheric correction algorithm for SeaWiFS

The TOA reflectance at wavelength λ, $\rho_{\mathrm{TOA}}(\lambda)$ is defined as equation (1), where $f_0(\lambda)$ is the mean extraterrestrial solar irradiance, θ_S is the solar-zenith angle and σ is the sun-earth distance coefficient. $L_{TOA}(\lambda)$ is the total upward radiance in the given viewing direction, and multiplying $L_{TOA}(\lambda)$ by π is due to the assumption of Lambertian surface.

$$\rho_{TOA}(\lambda) = \frac{\pi \times L_{TOA}(\lambda)}{F_0(\lambda) \times \cos(\theta_S)}$$
$$F_0(\lambda) = \mathrm{f}_0(\lambda) \times \sigma(\mathrm{Jday}) \tag{1}$$

To estimate σ, there are various sun-earth distance models and we adopted Spencer (1971) model that defined as equation (2) (Fig. 7.).

$$\begin{aligned}\sigma(\mathrm{Jday}) = 1.00011 &+ 0.034221 \times \cos\left(2\pi \frac{\mathrm{Jday}-1}{365}\right) \\ &+ 0.00128 \times \sin\left(2\pi \frac{\mathrm{Jday}-1}{365}\right) \\ &+ 0.000719 \times \cos 2\left(2\pi \frac{\mathrm{Jday}-1}{365}\right) \\ &+ 0.000077 \sin 2 \times \left(2\pi \frac{\mathrm{Jday}-1}{365}\right)\end{aligned} \tag{2}$$

where Jday is *julian day*

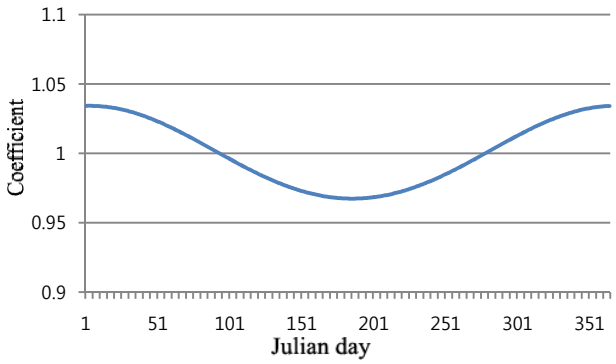

Fig. 7. Result of earth-sun distance model

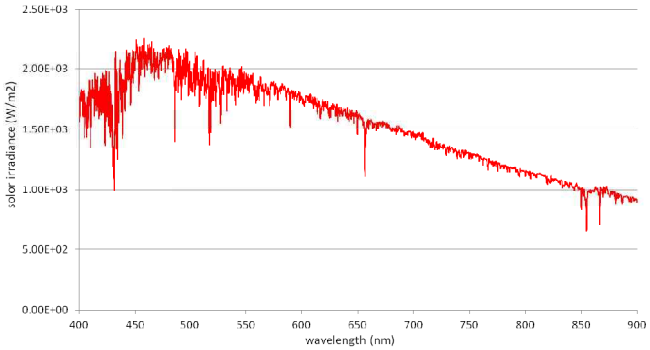

Fig. 8. Mean solar radiation

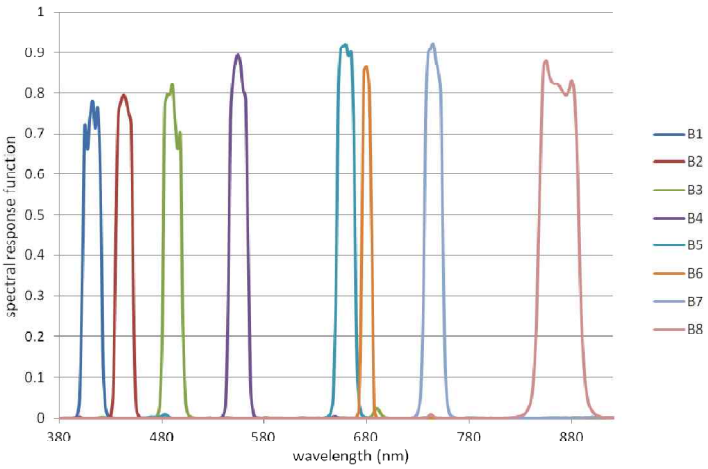

Fig. 9. Spectral response function of GOCI

And we used Thuillier's measurement (Thuillier et al., 2003) for $f_0(\lambda)$ values (Fig. 8.), and this hyperspectral data was converted into GOCI's band spectral values by equation

(3) (Fig. 9.).

$$f_0(b_i) = \frac{\int f_0(\lambda)\Theta_i d\lambda}{\int \Theta_i d\lambda} \quad (3)$$

where b_i is a band considered spectrum and Θ_i is the spectral response function of the sensor for a band *i*.

By this equation, converted f_0 values are listed in the Table 3.

Band number (center wavelength λ)	1 (412 nm)	2 (443 nm)	3 (490 nm)	4 (555 nm)	5 (660 nm)	6 (680 nm)	7 (745 nm)	8 (865 nm)
$f_0(\lambda)$ value unit: $w/m^2/um/sr$	1738.8	1922.1	1988.4	1869.9	1535.3	1508.3	1295.9	967.6

Table 3. GOCI band considered $f_0(\lambda)$ values

$\rho_{TOA}(\lambda)$ can be partitioned linearly into various distinct physical contributions as equation (4). $\rho_{TOA}(\lambda)$ is composed of pure ocean reflectance without surface's Fresnel reflectance $\rho_w(\lambda)$, the pure molecular multiple scattering reflectance (in the absence of air aerosol particles) $\rho_r(\lambda)$, the pure aerosol scattering reflectance of air molecules absences $\rho_a(\lambda)$, the multiple scattering reflectance between molecules and aerosol interaction $\rho_{ra}(\lambda)$, the sea surface's specular reflectance of sunlight $\rho_g(\lambda)$, and $\rho_{wc}(\lambda)$ is the whitecap reflectance component. $T(\lambda)$ is the atmospheric direct transmittance from sea surface to the sensor and $t'(\lambda)$ is the upward diffuse transmittance of atmosphere from the sea surface to the sensor. In this terms, the point of atmospheric signals as the $\rho_r(\lambda)$, the $\rho_a(\lambda)$ and the $\rho_{ra}(\lambda)$ is, this signals contains not only the direct scattering reflectance ((a) of Fig. 10.) but also the Fresnel bounced air reflectance. ((b) and (c) of Fig. 10.)

$$\rho_{TOA}(\lambda) = \rho_r(\lambda) + \rho_a(\lambda) + \rho_{ra}(\lambda) + T(\lambda)\rho_g(\lambda) + t'(\lambda)\rho_{wc}(\lambda) + t'(\lambda)\rho_w(\lambda) \quad (4)$$

To correctly derive $\rho_w(\lambda)$ from the right side of equation (4), it is necessary to estimate the other terms accurately.

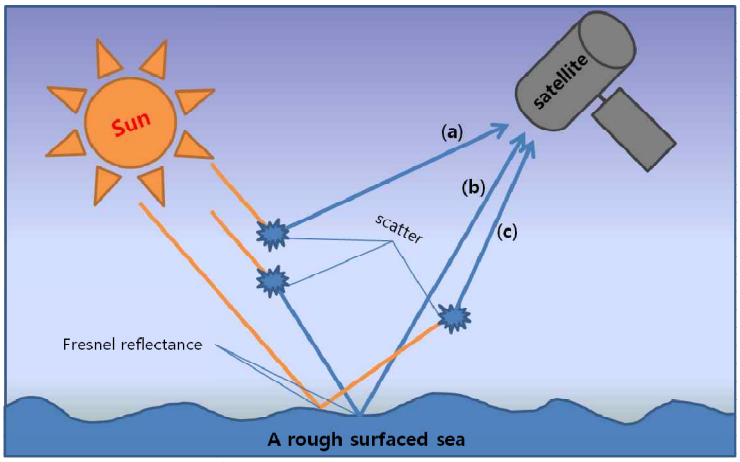

Fig. 10. Components of atmospheric reflectances

Correction for the Rayleigh reflectance

$\rho_r(\lambda)$ is the component of molecular scattering in the air. It can horizontally fluctuate due to air pressure changes, different scattering angles, different mixing ratios of air molecule components, and changes in the wind field distribution of the sea surface. We have to consider all of these factors to correctly estimate the Rayleigh scattering reflectance term. In the general cases, Rayleigh reflectance is the major quantitative part of the atmosphere. We can easily estimate the value within 1% of error by practical homogenization of its horizontal fluctuation (Gordon et al., 1988).

There are many ways to estimate the Rayleigh scattering reflectance, and using the radiative transfer theory is the most prevalent. It is computationally intensive to directly calculate each pixel's Rayleigh reflectance, and thus interpolated data from a pre-computed four-dimensional lookup table of most major parameters for solar zenith angle, sensor zenith angle, relative azimuth angle, and wind speed (;have a correlation with surface Fresnel reflectance of Fig. 10.) are generally used (Gordon and Wang, 1992;

Wang, 2002). To simulate atmospheric reflectance, a molecular US62 atmosphere pressure and temperature profiles were applied. (McClatchey et al., 1971)

Molecular scattering reflectance change by the atmospheric pressure is easily estimated by equation (5) and (6) (Wang, 2005).

$$\rho_r^{corect}(\lambda,\chi,\theta_s,\theta_v) = \rho_r(\lambda) \times \frac{1.0 - e^{-coef_r(\lambda,\theta_s,\theta_v)\times\tau_r^{correct}(\lambda,\chi)\times m^{air}(\theta_s,\theta_v)}}{1.0 - e^{-coef_r(\lambda,\theta_s,\theta_v)\times\tau_r(\lambda)\times m^{air}(\theta_s,\theta_v)}} \quad (5)$$

where

$$coef_r(\lambda,\theta_s,\theta_v) = -\{0.6543 - 1.608\times\tau_r(\lambda)\} + \{0.8192 - 1.2541\times\tau_r(\lambda)\}\times\log(m^{air}(\theta_s,\theta_v))$$

$$, \quad \tau_r^{correct}(\lambda,\chi) = \left(\tau_r(\lambda)\times\frac{\chi}{1013.25}\right) \quad (6)$$

$$, \quad m^{air}(\theta_s,\theta_v) = \frac{1.0}{\cos\theta_s} + \frac{1.0}{\cos\theta_v}$$

where $\rho_r^{correct}$ is an air pressure corrected Rayleigh reflectance, where θ_V is sensor zenith angle and χ is an air pressure in *mb*

Correction for the Aerosol reflectance

The aerosol terms that stand for $\rho_{ra}(\lambda)+\rho_a(\lambda)$ from the equation (4) are significantly changed in space and time. Thus it is a key element in the atmosphere correction to more accurately estimate the aerosol reflectanc. The first atmospheric correction algorithm used the black pixel assumption that the NIR ocean reflectance are negligible compared to aerosol reflectance (Gordon, 1978). This first method also assumes that aerosol particles are scattered by photons only once. The single scattering reflectance can be expressed as equation (7), where $\rho_{as}(\lambda)$ is the aerosol single scattering reflectance, $\omega_a(\lambda)$ is the aerosol's single scattering albedo, $\tau_a(\lambda)$ is the aerosol optical thickness and $P_a(\lambda)$ is the aerosol's scattering phase function. And $r(\theta_S)$ and $r(\theta_V)$ are the surface's Fresnel reflectance term of

the solar zenith angle and sensor zenith angle that could be induced by (b) and (c) of Fig.10.

$$\rho_{as}(\lambda) = \frac{\omega_a(\lambda)\tau_a(\lambda)\left[P_a(\lambda,\Theta_+) + P_a(\lambda,\Theta_-)\{r(\theta_S) + r(\theta_V)\}\right]}{4\cos(\theta_S)\cos(\theta_V)}$$

$$\cos(\Theta_\pm) = \pm\cos(\theta_V)\cos(\theta_S) + \sin(\theta_V)\sin(\theta_S)\cos(\phi_V - \phi_S) \qquad (7)$$

Because the spectral shapes are always same over different aerosol's optical thickness with this single scattering assumption, we could easily estimate them for aerosol reflectance at all wavelengths. In the real world however, the light can be scattered multiple times by aerosols and cause more errors at shorter wavelengths or a higher optical path. Wang (1991) found a near-linear relationship between single scattered and multiple scattered reflectance. These can be converted forward and backward for each aerosol model and geometric angles. Gordon and Wang (1994) developed a multiple scattering based atmospheric correction process that follows flowchart in Fig. 11.

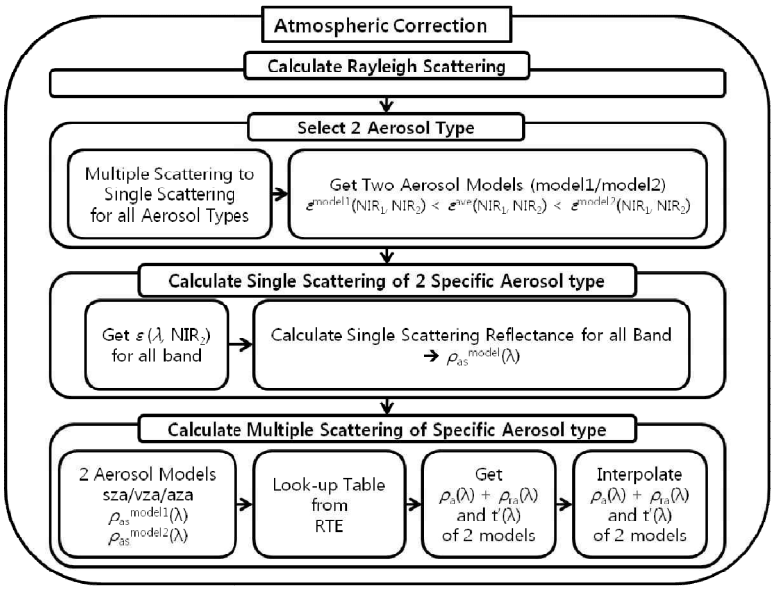

Fig. 11. Process of removing aerosol reflectance

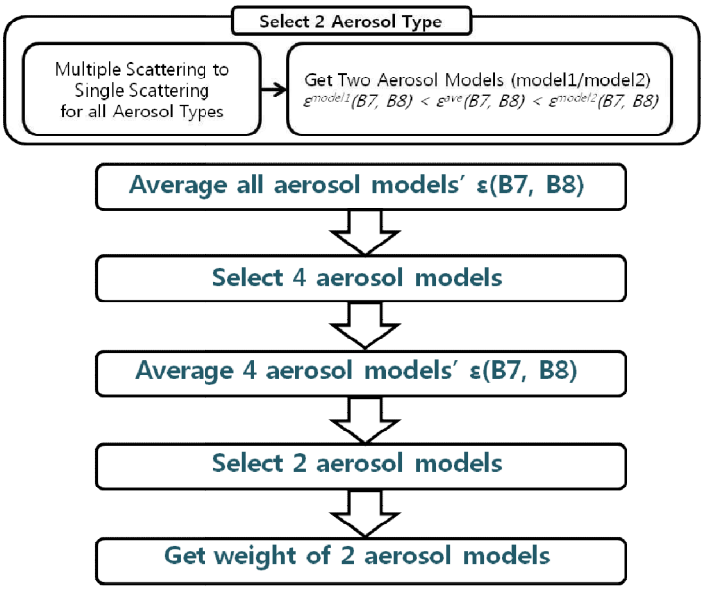

Fig. 12. Flowchart of aerosol model selection

In this method, using two near infrared aerosol reflectances, $\rho_a(\mathrm{NIR}_1)+\rho_{ra}(\mathrm{NIR}_1)$ and $\rho_a(\mathrm{NIR}_2)+\rho_{ra}(\mathrm{NIR}_2)$, we convert these multiple scattered reflectances to single scattered reflectances for all aerosol models. To find a specific aerosol model of each pixel, we average all models' single scattering reflectance slope, and using the interpolated two nearest slopes of aerosol models as Fig. 12. By equation (8) derived from equation (7) or a simple single scattering reflectance model of aerosol as equation (9), we can easily find all other visible bands' single scattering reflectances for specific aerosol models (Gordon and Wang, 1994).

$$\rho_{as}(\lambda_1)/\rho_{as}(\lambda_2)=\frac{\omega_a(\lambda_1)\tau_a(\lambda_1)\left[P_a(\lambda_1,\Theta_+)+P_a(\lambda_1,\Theta_-)\{r(\theta_S)+r(\theta_V)\}\right]}{\omega_a(\lambda_2)\tau_a(\lambda_2)\left[P_a(\lambda_2,\Theta_+)+P_a(\lambda_2,\Theta_-)\{r(\theta_S)+r(\theta_V)\}\right]} \quad (8)$$

$$\rho_{as}(\lambda_1)/\rho_{as}(\lambda_2)=e^{c(\lambda_2-\lambda_1)} \quad (9)$$

Then, as we know the $\rho_{as}(\lambda)$ and aerosol model, we can revert $\rho_a(\lambda)+\rho_{ra}(\lambda)$ for all bands by

the aerosol single scattering and multiple scattering relationships. Aerosol removal and model selection results are shown as Fig. 13.

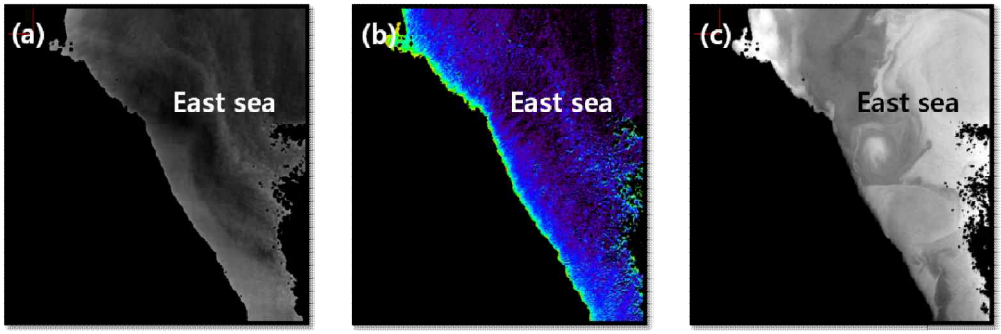

Fig. 13. Result of aerosol correction, (a) is a Band 7 and 8 signal image (aerosol signal), (b) is an aerosol model distribution, (c) is an aerosol removed signal image at 443 *nm* wavelength

Aerosol models

The aerosol models for the atmospheric correction are similar for all ocean aerosol cases. The general atmospheric correction uses several aerosol models, such as Shettle and Fenn (1979)'s maritime model with relative humidity (RH) 50%/70%/90%/99% (denoted M50, M70, M90, M99), coastal model with RH 50%/70%/90%/99% (denoted C50, C70, C90, C99), tropospheric model with RH 50%/80%/99% (denoted T50, T80, T99), oceanic model with RH 99% (denoted O99) models. These 12 aerosol models represent non- or weakly-absorbing aerosols and models (e.g. $\omega_a(865nm)$ varies from 0.93 for T50, to 1.0 for O99) are made by composition of aerosol components such are water soluble, dustlike, sea salt, soot and water (e.g. maritime aerosol is constructed by combining 98.7% of water soluble and 1.3% of sea salt). The physics of the scattering such are single scattering albedo, scattering phase function and aerosol optical thickness can be derived by Hulst (1957) when an aerosol model's microphysical and optical properties are given (i.e., size distribution and complex index of refraction).

Estimation of whitecap reflectance

The whitecap reflectance correction is also important and can be affected by terms such as the wind field and surface temperature. Normally, only considering the wind field (the major term for whitecap correction) is enough (Blanchard, 1971). This can be expressed as equation (10), the wavelength-independent model (Gordon and Wang, 1994), where $[\rho_{wc}]_N$ is the normalized whitecap reflectance, w is wind speed (m/s)

$$[\rho_{wc}]_N = 0.649 \times 10^{-6} \times w^{3.52} \tag{10}$$

Fig. 14. shows the relationship between the wind speed and the whitecap reflectance. For cases of wind speed under 8 m/s, the whitecap reflectance is generally negligible.

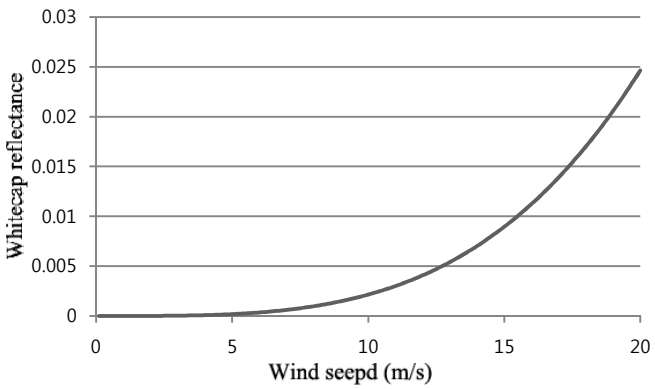

Fig. 14. The relationship between the wind speed and the whitecap reflectance

Estimation of sun-glint

Sun-glint is the specular reflectance of sunlight by roughened ocean surface. For the GOCI's viewing angle, the sun-glint effect is small even in the summer. Nevertheless sun-glint effect in GOCI data is less than other polar orbit sensors, a small direct reflectance of sunlight by ocean surface can cause a considerable error during atmospheric correction because the sun light itself is still massive. Typically, the model of Cox & Munk (1955) is used to remove the sun-glint effect ρ_g, and denoted as equation (11) where ω is the specular reflection angle, θ_n is reflected direction and $p(z_x, z_y)$ is the probability

distribution of facet slopes that depends on the wind speed and direction.

$$\rho_g = \frac{\pi f(\omega,\lambda)\, p(z_x, z_y)}{4\cos\theta_v \cos\theta_s \cos^4\theta_n} \tag{11}$$

Where $\cos 2\omega = \cos\theta_v \cos\theta_s + \sin\theta_v \sin\theta_s \cos(\phi_v - \phi_s)$,

$$\cos\theta_n = \frac{\cos\theta_v + \cos\theta_s}{2\cos\omega}$$

Applying the atmospheric transmittance

There are typically two cases of transmittance. One is the direct (or beam) transmittance $T(\lambda)$ used for some narrow angle affected cases, such as the sun-glint term. This transmittance is consisted of molecular term and aerosol term, and can be expressed as : $T(\lambda) = t_r(\lambda) \times t_{oz}(\lambda) \times t_a(\lambda) \times t_{NO_2}(\lambda)$

The other is the diffuse transmittance $t'(\lambda)$ applied for general ocean surface terms that can be defined as : $t'(\lambda) = td_r(\lambda) \times td_{oz}(\lambda) \times td_a(\lambda) \times td_{NO_2}(\lambda)$

The atmospheric transmittance depends on an attenuation coefficient i.e. affected again by absorbing matter such as ozone and nitrogen dioxide, and scattering matter such as air molecular and aerosol particles. An estimation of the atmospheric molecular beam transmittance with no absorption can be expressed as equation (12). The diffuse transmittance with no absorption can be expressed as equation (13), which is based on the molecule's symmetric scattering phase function. Rayleigh optical thickness $\tau_r(\lambda)$ computed from equation (14) of Gordon et al.(1988).

$$t_r(\lambda) = e^{\frac{-\tau_r(\lambda)}{\cos(\theta_r)}} \tag{12}$$

$$td_r(\lambda) = e^{\frac{-\tau_r(\lambda)}{2\cos(\theta_r)}} \tag{13}$$

$$\tau_r(\lambda) = 0.008569 \times \lambda^{-4} \times \left\{1.0 + (0.0113 \times \lambda^{-2}) + (0.00013 \times \lambda^{-4})\right\} \tag{14}$$

The aerosol's transmittance estimation method also can be expressed using the beam transmittance model (15) and the diffuse transmittance model (16) by Gordon et al. (1983) where $\zeta(\lambda)$ is the forward scattering probability of aerosol particle.

$$t_a(\lambda) = e^{\frac{-\tau_a(\lambda)}{\cos(\theta_V)}} \tag{15}$$

$$td_a(\lambda) = e^{\left[\frac{-\{1-\omega_a(\lambda)\zeta(\lambda)\}\times\tau_a(\lambda)}{\cos(\theta_V)}\right]} \tag{16}$$

Approximations using only absorption are easily expressed as equation (17) and (18) for beam and diffuse transmittance.

$$td_{oz}(\lambda) = t_{oz}(\lambda) = e^{\frac{-\tau_{oz}(\lambda)}{\cos(\theta_V)}} \tag{17}$$

$$td_{NO_2}(\lambda) = t_{NO_2}(\lambda) = e^{\frac{-\tau_{NO_2}(\lambda)}{\cos(\theta_V)}} \tag{18}$$

Correction of Bidirectional Reflectance Distribution Function effect

To derive more accurate satellite retrievals such as normalized water-leaving radiance (nL_w) or remote sensing reflectance (Rrs) from the ocean reflectance $\rho_w(\lambda)$, bidirectional reflectance distribution function (BRDF) correction is needed. Generally BRDF of sea surface does not take a large part of atmospheric correction. Therefore Lambertian surface assumption and neglect of Fresnel effect are commonly acceptable. When solar zenith angle or satellite zenith angle increase (~50˚) , however, BRDF correction should be accounted. BRDF can be considered by its component such as sea surface's Fresnel effects and constituent of particles beneath the water surface. In the case of the lower zenith angle, BRDF effects are dominated by the water constitutes. In contrast the higher zenith angle case, BRDF is more affected by the sea surface's Fresnel effect (Park and Ruddick, 2005).

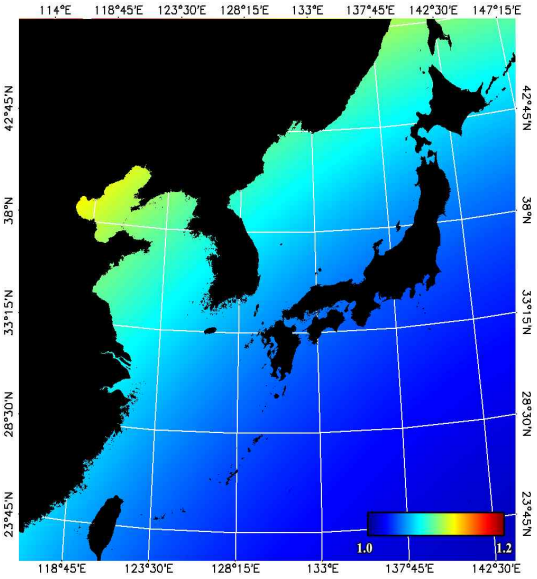

Fig. 15. Result of total BRDF effect correction coefficient

(2011/10/27 09:16 Local time, 412*nm*)

Fresnel effect correction can be considered by satellite zenith angle and solar zenith angle. Generally the downward Fresnel effect of BRDF ($E_d^{0-}(\lambda)/E_d^{0+}(\lambda)$) that can be dominated by solar angle is corrected by interpolation of pre-computed LUT, and this LUT is made by result of radiative transfer theory based simulation with geometric angle, wind speed, water constituent and AOT (Wang, 2006). Upward Fresnel transmittance coefficient $t_{surface}$ by satellite elevation angle change can be simply corrected by equation (19) where $t_w(\theta_v)$ is Fresnel transmittance of air-sea interface (Franz et al., 2003). Fig. 15. is a GOCI's band 1 (412*nm*) BRDF correction result for October 27th, (09:16 in local time).

$$t_{surface}(\theta_v) = \frac{0.9795218}{1.0 - t_w^f(\theta_v)}$$
$$where,\ t_w^f(\theta_v) = \frac{t_w(0°)}{t_w(\theta_v)} \qquad (19)$$

2.2. Extension of the SeaWiFS Standard Atmospheric Correction Algorithm to the GOCI

Slot Correction

GOCI acquires images by the step-and-stare method. The one frame image is called as a slot. A L1B image consists of 16 slot image. This is contrasted to the cross-track scanning method of the general polar orbit sensor. Each slot is captured in a sequence with time interval of about 102 seconds. This time difference between each slot results in difference in the computed solar angles. We accounted for the time difference effect in two major terms, the downward solar irradiance and scattering angle change of each slot. In this study, we recalculated these two major terms per slot. The changes are shown in Fig. 16.

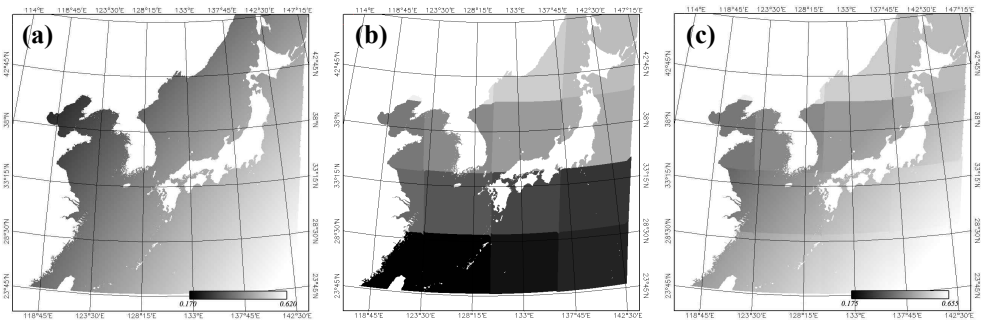

Fig. 16. Illustration of the slot correction for $\cos(\theta_S)$. (a) $\cos(\theta_S)$ value without slot correction, (b) GOCI slot area, (c) $\cos(\theta_S)$ value with slot correction

Mask of unavailable pixels

Earlier studies, mask had accounted for only the high aerosol optical thickness (AOT) or clouds. In this cases, the simplest way of removing cloud or high AOT is only use threshold of ρ_{TOA}(NIR) - ρ_r(NIR), with the underlying assumption that high absorbance of water at NIR wavelengths. However, since the ocean colour remote sensing had been considered in turbid coastal waters, those masks over turbid waters should be also considered. For highly turbid waters, ocean has a considerable reflectance by the backscattering of suspended sediment. Thus only use threshold of a band's reflectance over turbid waters is no more valid. To separate turbid water and a high AOT, it is needed

to use multiple bands. In this study, we used two NIR bands' (745 nm and 865 nm) slope and threshold of ρ_{TOA}(NIR) - ρ_r(NIR) value of the GOCI based on the theory of water's absorption always make two NIR wavelengths' slope higher than the aerosol's slope, and these threshold values were decided by a simple test based method. We approximate that reflectance ratio of ocean's two NIR bands' is always same (Ruddick et al., 2006) and give constraint that aerosol's slope range is around 0.9 to 1.2 from the assumption of aerosol types are only the oceanic or maritime. Selected pixels by threshold are applied to around 3x3 pixels due to the removal of sparkles that coming from the cloud's movement during band change. The result of this mask method is shown as the Fig. 17.

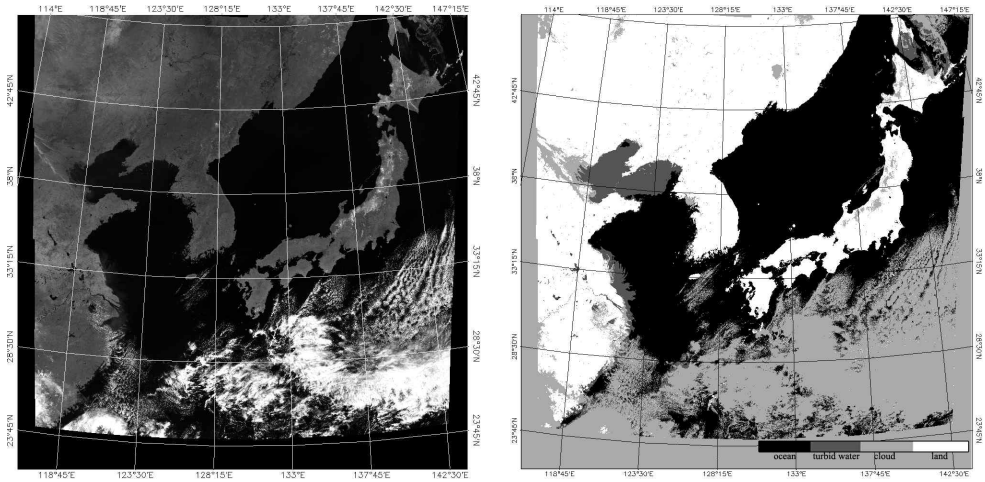

Fig. 17. Result of cloud and turbid water masking

Aerosol models and building LUT for GOCI

Image size of GOCI's standard level 1B data is totally about 2.5×10^8 pixels (5567 columns, 5685 lines, 8 bands), and this huge size of data increases processing time of atmospheric correction. Furthermore, aerosol models occasionally cross over in $\rho_{as}(\lambda)/\rho_{as}(865nm)$ space under certain geometric conditions as Fig. 18. These cause discontinuous lines along constant scattering angles (Wang, 2002). While the SeaWiFS atmospheric correction algorithm uses 12 aerosol models, GOCI adopted only 3 aerosol models such are M99, M50 and C50 to avoid image discontinuity and running time problem. We build 3-dimension LUTs of each aerosol models with resolution of

10×10×19 (10×cos(θ_S), 10×cos(θ_V), 19× (ϕ_S-ϕ_V)). Aerosol model's size distribution and complex index of refraction were derived by Shettle and Fenn (1979) and Hess et al. (1998). Scattering phase function, single scattering albedo, and optical thickness were computed using the Optical Properties of Aerosols and Clouds (OPAC) package (Hess et al., 1998), and radiative transfer simulation for derive relationship between single scattering and multiple scattering was performed by the Second Simulation of a Satellite Signal in the Solar Spectrum - vector (6SV) software (E. Vermote et al., 2006).

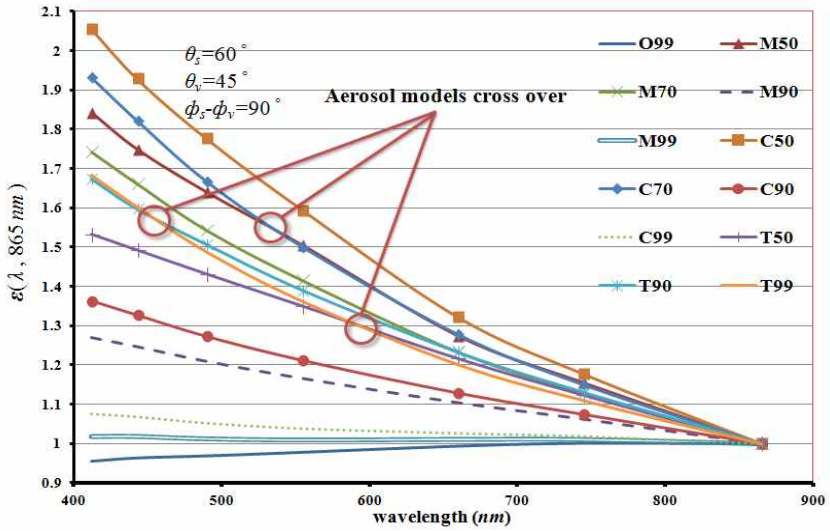

Fig. 18. Aerosol models can cross over in $\rho_{as}(\lambda)/\rho_{as}(865nm)$ space under certain geometric conditions

Validation of the atmospheric correction with reduced aerosol models showed acceptable results with this optimization. Fig. 19. provides comparison result between using 12 aerosol models with high definition LUT (35 of cos(θ_S), 35 of cos(θ_V), 19 of (ϕ_S-ϕ_V)) and using 3 aerosol models with low definition LUT.

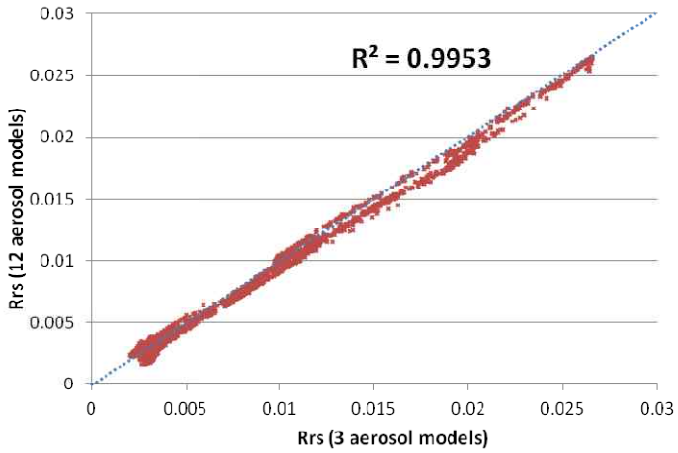

Fig. 19. Comparison result of atmospheric correction between 12 aerosol models with a high definition LUT and 3 aerosol models with a low definition LUT

Near infrared ocean reflectance correction for case-2 water cases

For highly turbid waters such as coastal waters or estuary of river, the black pixel assumption is no longer valid. This invalidity can seriously overestimate quantity of aerosol during the atmospheric correction. To solve this problem, several techniques have been proposed (e.g., the fixed aerosol type method (Ruddick et al., 2000), nearest non-turbid pixel (Hu et al., 2000), and the iterative method between ocean reflectance model and atmospheric correction (Siegel et al., 2000).

In this study, we developed a new iterative method for the correction of NIR ocean reflectances. We used an empirical relationship in the red (660 nm) to two NIR bands (745 and 865 nm) for the ocean reflectance model. Recent research has shown that the reflectance between the red and NIR bands have a nearly linear relationship with the total suspended sediment. However, for extremely high turbidity cases, the relationship changes to non-linear by saturation of the red band (Neukermans et al., 2008; Wang et al., 2012). We found a simple empirical relationship of normalized ocean reflectance $[\rho_w(\lambda)]_N$ that defined as $\rho_w(\lambda)/\cos(\theta_S)$. We used a simple non-linear polynomial model for the relationship between $[\rho_w(660\text{nm})]_N$ and $[\rho_w(745\text{nm})]_N$, and adopted a fixed 1.94 ratio for

the $[\rho_w(745nm)]_N$ and $[\rho_w(865nm)]_N$ based on Ruddick et al. (2006).

To build an empirical NIR correction model, we used satellite-derived data, which reduced errors such as from the above-water measurement and ship effects. In this study, we derived the turbid ocean reflectance from the nearest non-turbid atmospheric correction (Hu, 2000). The fluctuating random errors of the aerosol's NIR reflectances were counterbalanced by the long-term data averaging during empirical modeling. Thus the satellite derived relationship showed lower scatter than the in-situ measurement-based relation Fig. 20.

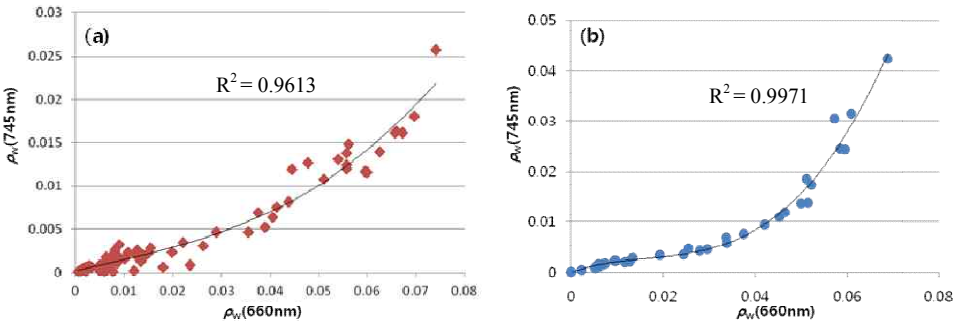

Fig. 20. Relationship of the red and NIR water reflectances. (a) *In situ* derived relationship, (b) Satellite derived relationship

From the scatter plot of Fig.20., we found an empirical polynomial between $[\rho_w(660nm)]_N$ and $[\rho_w(745nm)]_N$ that can be expressed as equation (20)

$$[\rho_w(745nm)]_N = \sum_{n=1}^{4} C_n [\rho_w(660nm)]_N^{\,n} \qquad (20)$$

And a relationship between $[\rho_w(745nm)]_N$ and $[\rho_w(865nm)]_N$, we used a constant based on the water's strong absorption of NIR. This constant relationship is acceptable for overall turbid waters. (Ruddick et al., 2006)

Our approach showed improved results for the separation of aerosols and case-2 water reflectance. Fig. 21. shows $\rho_{ra}(555nm) + \rho_a(555nm)$ over the Yeong-san Riverestuary, representing a highly turbid case. By the black pixel assumption atmospheric correction,

coastal adjacency turbid water always mistake ocean reflectance for aerosol reflectance as red circled area of Fig.21.(a). In our NIR correction method as (b) of Fig.21., we can see a better separation between the aerosol and ocean over the turbid areas.

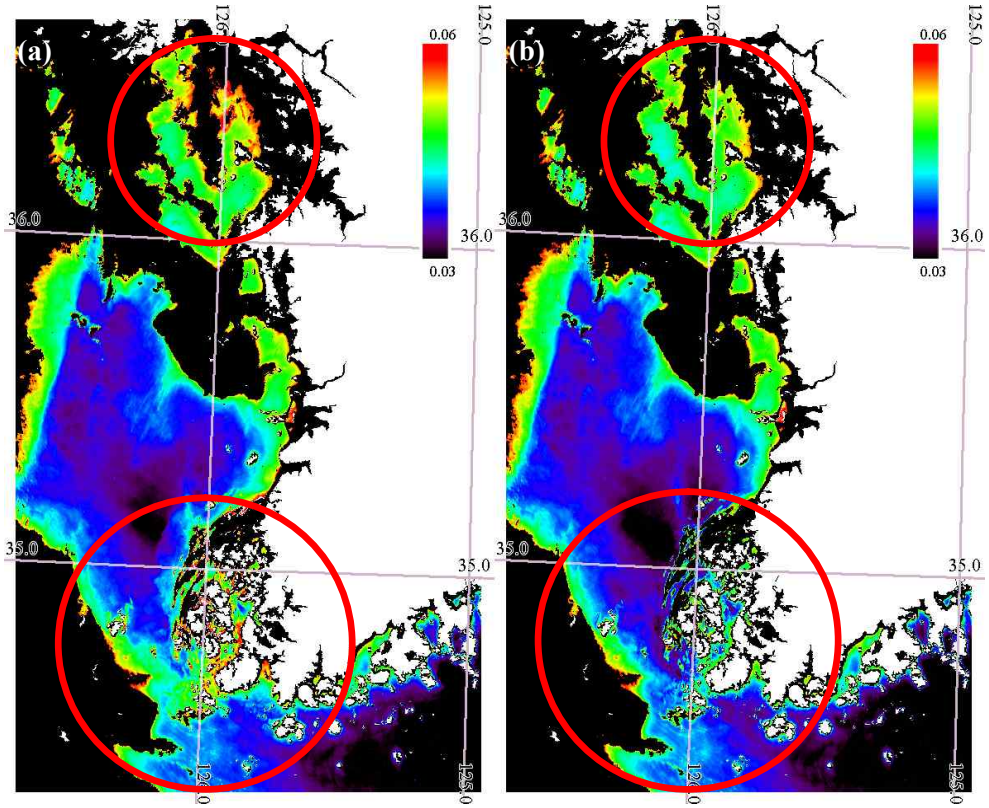

Fig. 21. Comparison of the aerosol reflectance. ρ_a(555 *nm*)+ρ_{ra}(555 *nm*) computed with (a) the black pixel assumption, and (b) the NIR correction model. The NIR corrected model shows improved estimation of the aerosol reflectance in two turbid water area, Gyeonggi-bay (upper circle) and the south-east coastal waters (lower circle).

3. Results

Some sample GOCI images using the new atmospheric correction algorithm are shown from Fig. 22 to 24. Fig. 22 is a composited true color image of TOA radiance (left) and normalized water-leaving radiance (right). Fig. 23 shows the TOA radiance image of GOCI that contains Rayleigh radiance and aerosol radiance. Fig.24 is a normalized water-leaving radiance image using the new of atmospheric correction method.

For a validation, we used *in situ* data from a cruise in 2011 of the East Sea, around Young-san River estuary and the East China Sea as Fig.25. Masked or flagged stations such are high solar zenith angle, cloud edge, land adjacency, high turbidity over the threshold and high AOT exceeds the threshold were excluded.

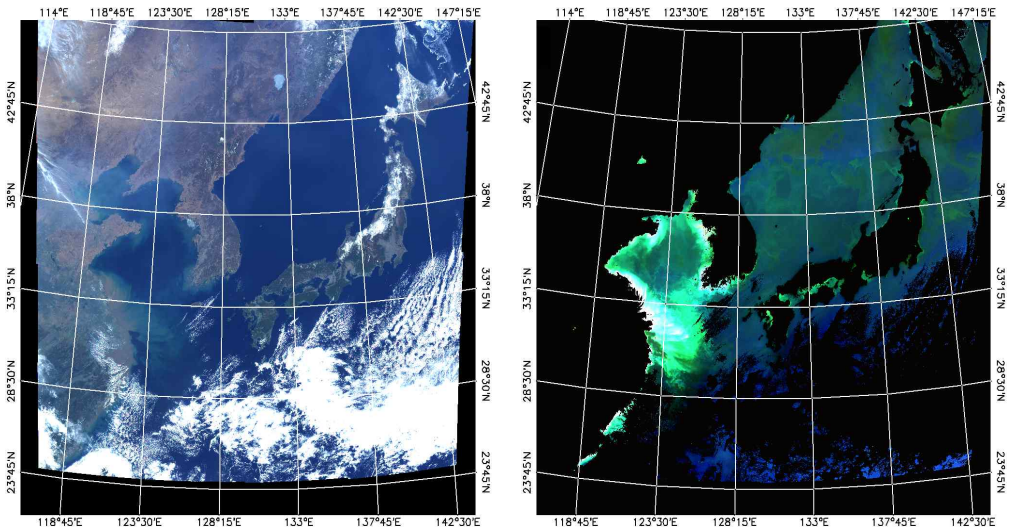

Fig. 22. RGB composite true color images of TOA radiance before atmospheric correction (left) and nLw image as a result of atmospheric correction (right).

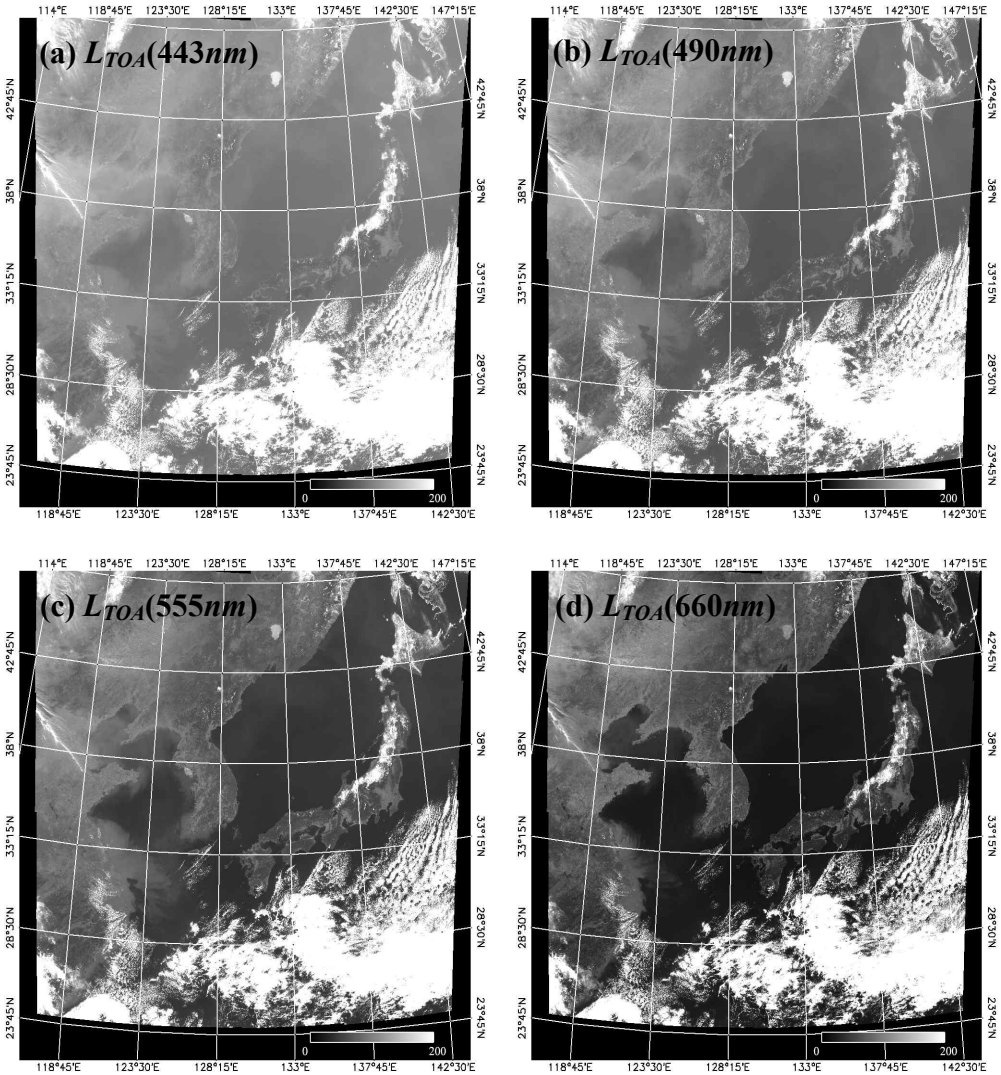

Fig. 23. TOA radiance images of each band (443*nm*, 490*nm*, 555*nm*, 660*nm*) before atmospheric correction. (unit : $w/m^2/um/sr$)

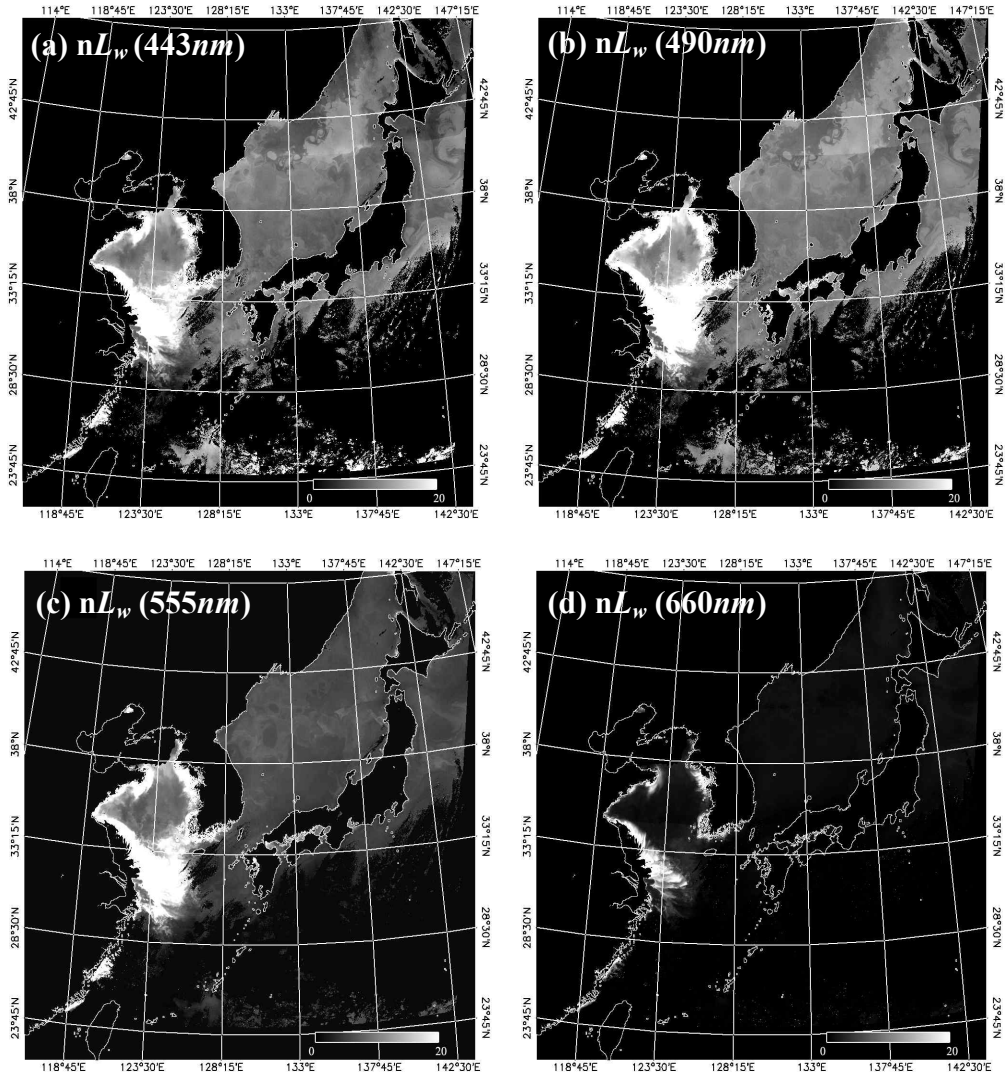

Fig. 24. nLw images of each band (443 *nm*, 490 *nm*, 555 *nm*, 660 *nm*) as a result of atmospheric correction. (unit : $w/m^2/um/sr$)

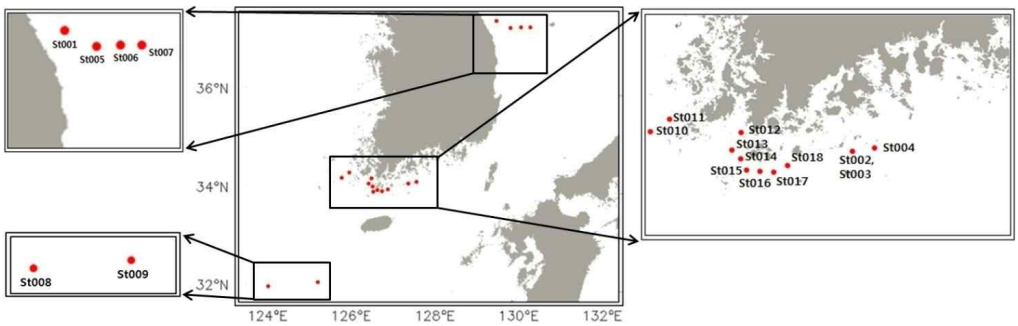

Fig. 25. Locations of the nLw match-ups from various cruises in 2011.

Above-water radiometry

Above water radiance spectra were measured by ASD FieldSpec and TriOS RAMSES hyperspectral radiometers. To reduce optical environmental uncertainties, the measurements were taken 5 times of every 1 second scanning. According to the NASA protocols (Mueller et al., 2003), total above-water spectra measurement of sea surface $L_{sea}^{0+}(\lambda)$ and sky radiance $L_{sky}(\lambda)$ with known geometric angles and can be used to derive water-leaving reflectance $\rho_w(\lambda)$ as follows:

$$\rho_w(\lambda) = \pi \frac{L_{sea}^{0+}(\lambda) - 0.0256 L_{sky}(\lambda)}{E_d^{0+}(\lambda)} \tag{21}$$

where equation $E_d^{0+}(\lambda)$ is the down-welling irradiance above the water.

Uncertainty in surface roughness by wind stress, inhomogeneous distribution of skylight and the ship's pitching can bring out the estimation error (η) of the Fresnel-reflected sky radiance. At the clear water, sky glint can be easily corrected by supposing that water-leaving reflectance at NIR (~870nm) is zero. For turbid water cases, however, atmospheric correction algorithm that based on the assumption of zero water-leaving reflectance at NIR wavelength has a serious defect where this assumption is no more valid. The shape of water-leaving reflectance spectra in NIR bands (720 nm ~ 900 nm) has the similar spectrum due to the strong water absorption at NIR wavelengths. By using this similarity, sky glint (η) in highly turbid waters can be corrected by following

(Ruddick et al., 2005 and 2006) :

$$\eta = \frac{\alpha_{1,2}\rho_w(NIR_2) - \rho_w(NIR_1)}{\alpha_{1,2} - 1}$$
$$\alpha_{1,2} = \rho_{wn780}(NIR_1) / \rho_{wn780}(NIR_2) \quad (22)$$

We selected 720*nm* and 780*nm* wavelengths for pair of NIR_1 and NIR_2, and calculated value of $\alpha_{1,2}$ is 1.35 by Ruddick et al.(2006). Wavelengths NIR_1 and NIR_2 must be chosen by the avoidance of gaseous and colored dissolved organic matter (CDOM) absorption. $\rho_{wn780}(\lambda)$ is defined as equation (23) that dividing the reflectance by its value at 780*nm* :

$$\rho_{wn780}(\lambda) = \frac{\rho_w(\lambda)}{\rho_w(780nm)} \quad (23)$$

Fig. 26. is an example of sky glint correction result.

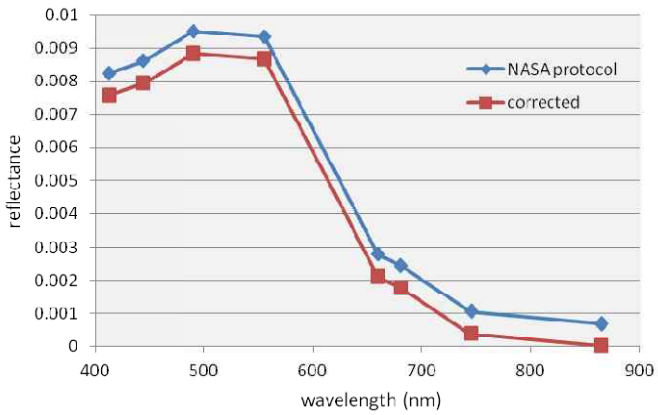

Fig. 26. Result of *in situ* sky glint correction.

Evaluation of the atmospheric correction for the GOCI

We compared GOCI derived normalized water leaving radiance (*nLw*) that denoted as equation (24) with *in situ* measurements.

$$nLw(\lambda) = \frac{[\rho_w(\lambda)]_N \times f_0(\lambda)}{\pi} \quad (24)$$

Fig. 27 and 28 are validation results and spectral comparisons for each station. Stations, St002 to St004 and St010 to St018 (Fig. 28) are relatively turbid waters. In these cases, we can see reasonable 1-to-1 matching results. However, GOCI derived *nLw* data in the stations in the East Sea which is characterized as clear open ocean waters, (St001 and St005 to St009 in Fig. 28), shows overestimated deviations. It seems that the overestimation comes from the above-water measurement error and an inaccurate calibration or an ancillary data error such like the wind speed, the O_3 concentration or atmospheric pressure that can cause atmospheric correction error (Andre and Morel, 1989; Gordon and Wang, 1992). Occasionally, some negative values appear at the red band (660nm) for clear waters (e.g., St001 or St008). These negative values mainly come from the aerosol model mismatching that can cause overestimation of aerosol reflectance.

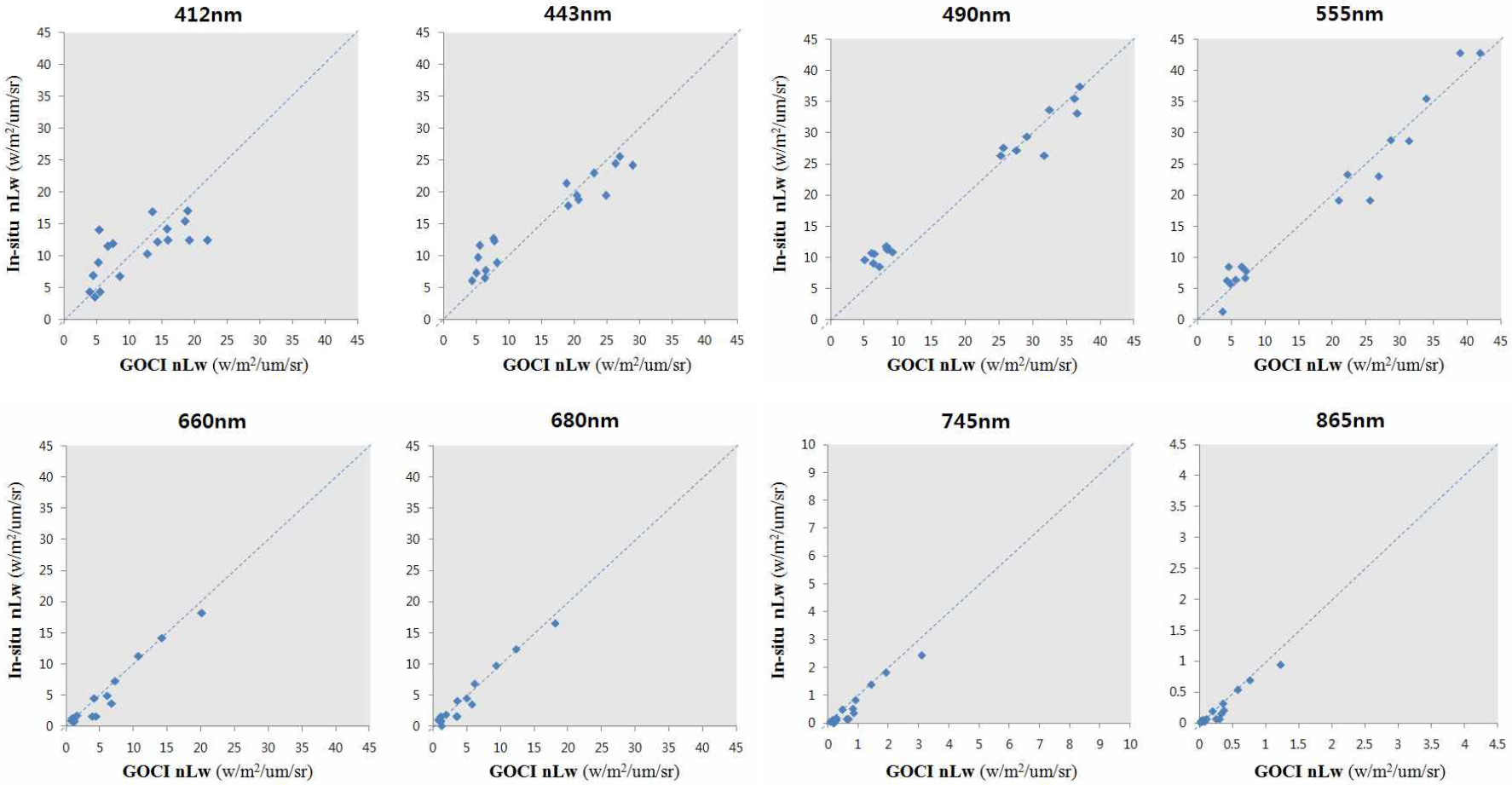

Fig. 27. Comparison between GOCI-derived and *in situ* nLw for each spectral band.

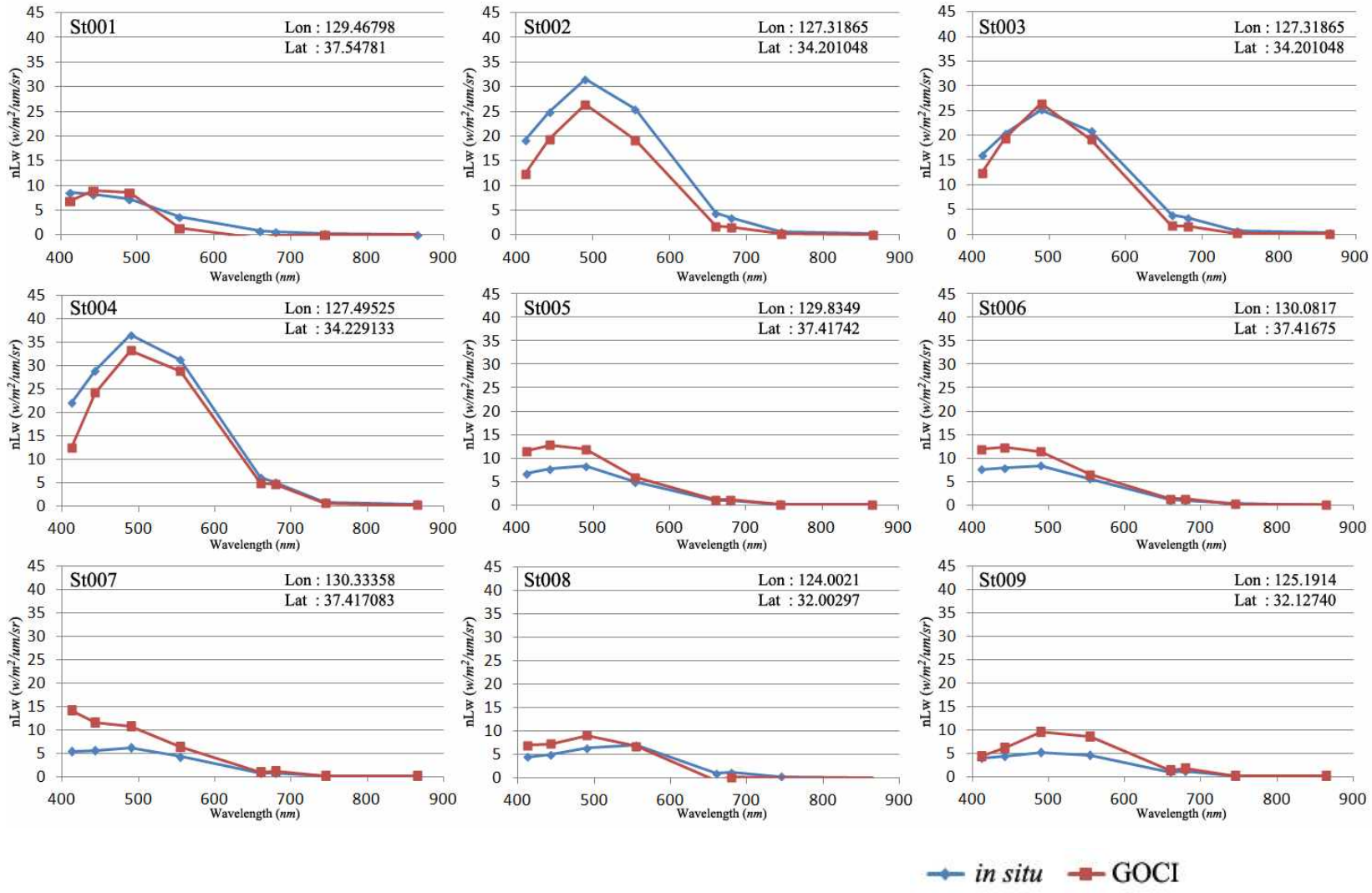

Fig. 28. Comparison between GOCI-derived and *in situ* nLw spectrum for each match-up (1).

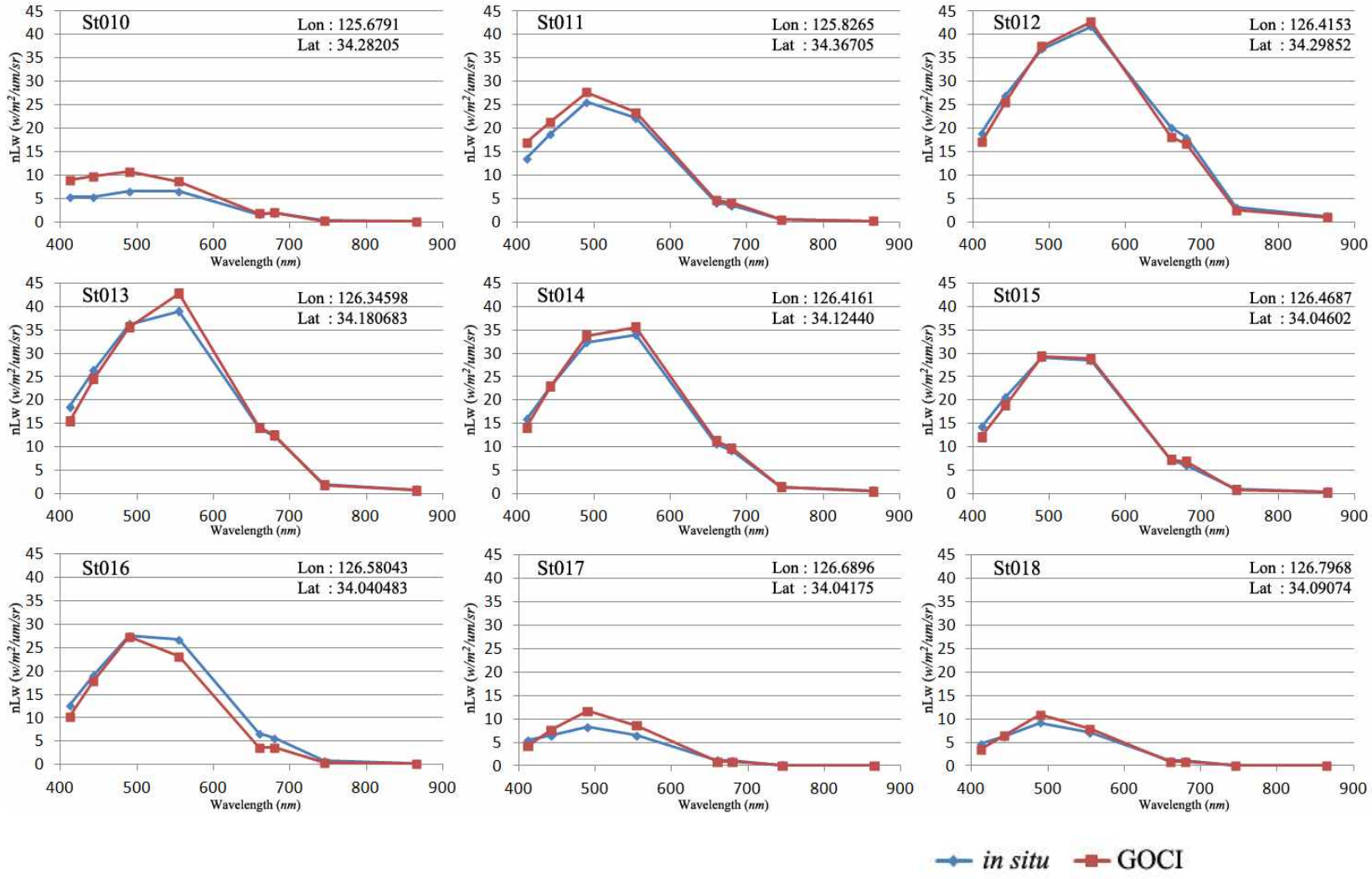

Fig. 28. Comparison between GOCI-derived and *in situ* nLw spectrum for each match-up (2).

4. Discussion and conclusions

Results from the match-up comparison between *in situ* and GOCI-derived nLw measurements show that the GOCI atmospheric correction algorithm reasonably works in both case-1 and case-2 waters. Particularly, the match-up results in the turbid waters are encouraging, indicating that the correction for NIR water reflectance works well. However, there are considerable discrepancies between *in situ* and GOCI-derived nLw measurements at blue to green bands in the relatively clear open ocean waters (low reflectance). The discrepancy would be possibly caused by uncertainties in the sensor calibration, aerosol models, the presence of the absorbing aerosols or above water nLw measuring errors of the field data. It should be noted that the results were obtained without vicarious calibration. A vicarious calibration can improve the atmospheric correction by forcing consistency between the sensor calibration and the atmospheric correction algorithm. Also, the nLw data (obtained from above-water measurements) in clear waters would be sensitive to the errors in the sky glint correction because of its low signal. More quality-controlled *in situ* nLw data for the clear waters are useful for validation of the atmospheric correction.

It is noted that there are some limitations in the GOCI atmospheric correction. The relationship between the red-NIR water reflectance is variable, depending on the absorption of suspended particles, chlorophyll or CDOM. Also the ocean reflectance at 660 nm wavelength can be saturated for extremely turbid cases like the estuary of the Yangtze River, which would cause an increasing error in estimation the NIR reflectance from 660nm. Other NIR bands around 709nm (Moore et al., 1999) or shortwave infrared (SWIR) bands (Wang, 2007) are useful for atmospheric correction in turbid waters, although there is no SWIR bands in GOCI, unfortunately. An absorptive aerosol can also cause underestimation of the ocean radiance. In spite that absorptive aerosols are often observed in the North East Asia (Lee et al., 2007; Lee and Kim, 2010), the classic atmospheric correction methods adopt no or less absorbed aerosol models, because it is unrealistic to distinguish absorbing aerosols and non-absorbing aerosols using only two NIR bands (Clark et al., 1997). There have been many efforts to solve this absorbed aerosol issue (Toratani et al., 2007; Wang, 2007), which showed decreased estimation error from 35% to 18% at 412*nm* (Fukushima et al., 2007) by use of shorter wavelengths (e.g., 380 or 400nm). However, GOCI does not have shorter wavelength bands. So it would be quite a challenge to extract ocean radiances correctly for the absorbing aerosol cases.

This thesis described an atmospheric correction algorithm for GOCI to be included in the next version of GDPS. Although the GOCI atmospheric correction algorithm showed encouraging results, it is under development and expected to be improved in future.

References

André J.M, Morel A (1991) Simulated effects of barometric pressure and ozone content upon the estimate of marine phytoplankton from space. J Geo Res 94:1029-1037

Austin R.W. (1974). The remote sensing of spectral radiance from below the ocean surface. Optical aspects of oceanography Academic Press : 317-344

Antoine D, Morel A (1998) Relative importance of multiple scattering by air molecules and aerosols in forming the atmospheric path radiance in the visible and near-infrared parts of the spectrum. Appl. Opt. 37:2245-2259

Antoine D, Morel A (1999) A multiple scattering algorithm for atmospheric correction of remotely sensed ocean color (MERIS instrument): principle and implementation for atmospheres carrying various aerosols including absorbing ones. Int. J. Remote Sens. 20:1875-1916

Blanchard D.C (1971) Whitecaps at sea. J Atmos Sci 28:645

Clark D.K, Gordon H.R, Voss K.J, Ge Y, Broenkow W, Trees C (1997) Validation of atmospheric correction over the oceans. J Geo Res 102(D14):17,209-17,217

Clark D.K, Gordon H.R, Voss K.J, Ge Y, Broenkow W, Trees C (1997) Validation of atmospheric correction over the oceans. J Geo Res 102(D14):17,209-17,217

Clarke G.K, Ewing G.C, Lorenzen C.J (1970) Spectra of backscattered light from the sea obtained from aircraft as a measure of chlorophyll. Science 167:1119-1121

Clarke G.L, Ewing G.C (1974) Remote spectroscopy of the sea for biological production studies. Optical aspects of oceanography Academic Press :389-413

E. Vermote, Tanre D, Deuze J.L, Herman M, Morcrette J.J, Kotchenova S.Y (2006) Second Simulation of a Satellite Signalin the Solar Spectrum-Vector (6SV). 6S User Guide Version 3

Thuillier G, Hersé M, Labs D, Foujols T, Peetermans W, Gillotay D, Simon P.C, Mandel H (2003)

Franz B.A, Eplee R.E, Bailey S.W, Wang M (2003) Changes to the atmospheric correction algorithm and retrieval of oceanic optical properties. SeaWiFS Postlaunch Technical Report Series 22:29-33

Fukushima H, Higurashi A, Mitomi Y, Nakajima T, Noguchi T, Tanaka T, Toratani M (1998) Correction of atmospheric effect on ADEOS/OCTS ocean color data : Algorithm Description and evaluation of its performance. J of Oceanography 54:417-430

Gordon H.R (1978) Removal of atmospheric effects from satellite imagery of the oceans. Applied Opt 17:1631–1636

Gordon H.R (1980). A preliminary assessment of the NIMBUS-7 CZCS atmospheric correction algorithm in a horizontally inhomogenous atmosphere. Gower J.F.R. (ed) Oceanography from Space. Plenum Press:281-294

Gordon H.R, Clark D.K (1980) Atmospheric effects in the remote sensing of phytoplankton pigments. Boundary-layer Meteorology 18: 299-313

Gordon H.R, Clark D.K, Brown J.W, Evans R.H Broenkow W.W (1983) Phytoplankton pigment concentrations in the Middle Atlantic Bight: comparison of ship determinations and CZCS estimates. Aplied Opt 22(1):20-36

Gordon H.R, Brown J.W, Evans R.H (1988) Exact Rayleigh scattering calculations for use with the Nimbus-7 Coastal Zone Color Scanner. Applied Opt 27(5):862–871

Gordon H.R, Wang M (1992) Surface-roughness considerations for atmospheric correction of ocean color sensors. I: The Rayleigh-scattering component. Applied Opt 31(21):4247–4260

Gordon H.R, Wang M (1994) Retrieval of water-leaving radiance and aerosol optical thickness over the oceans with SeaWiFS: a preliminary algorithm. Applied Opt 33(3):443–452

Gordon H.R, Wang M (1994) Influence of oceanic whitecaps on atmospheric correction of ocean-color sensors. Applied Opt 33(33):7754–7763

Hess M, Koepke P, Schult I (1998) Optical Properties of Aerosols and Clouds: The Software Package OPAC. Bulletin of the American Meteorological Society 79(5):831-844

Hu C, Carder K.L, Muller-Karger F.E (2000) Atmospheric Correction of SeaWiFS Imagery over Turbid Coastal Waters: A Practical Method. Remote Sens Environ 74:195–206

Hulst H.C (1957) Light scattering by small particles.

Lee K.H., Li Z, Wong M.S, Xin J, Wang Y, Zhao F (2007) Aerosol single scattering albedo estimated across China from a combination of ground and satellite measurements. J of Geophys Res 112:D22S15

Lee K.H, Kim Y.J (2010) Satellite remote sensing of Asian aerosols:a case study of clean, polluted, and Asian dust storm days. Atmos Meas Tech 3:1771-1784

McClatchey R.A, Fenn R.W, Selby J.E.A, Volz F.E, Garing J.S (1971) Optical properties of the Atmosphere. Env Res papers 354:AFCRL-TR-71-0279

Morel A. (1980) In-water and remote measuements of ocean color. Boundary-layer Meteorol. 18:177-201

Morel A, Maritorena S (2001) Bio-optical properties of oceanic waters : a reappraisal. J. Geophys. Res. 106(C4):7163-7180.

Moore G, J. Aiken, and Lavender S (1999) The atmospheric correction of water colour and the quantitative retrieval of suspended particulate matter in Case II waters: application to MERIS. *International Journal of Remote Sensing 20*(9):1713-1733.

Mueller J.L, Davis C, Arnone R, Frouin R, Carder K, Lee Z.P, Steward R.G, Hooker S, Mobley C.D, McLean S (2003) Above-water radiance and remote sensing reflectance measurements and analysis protocols. Ocean Opt protocol for satellite ocean color sensor validation Rev.4 3(3):21-31

Neukermans G, Ruddick K.G, Bernard E, Ramon D, Nechad B, Deschamps P.Y (2008) Mapping total suspended matter from geostationary satellites: a feasibility study with SEVIRI in the Southern North Sea. Opt Express 17(6):14029-14052

Park Y, Ruddick K (2005) Model of remote sensing reflectance including bidirectional effects for case1 and case 2 waters. Applied Opt 44(7):1236-1249

Ruddick K.G, Ovidio F, Rijkeboer M (2000) Atmospheric correction of SeaWiFS imagery for turbid coastal and inland waters. Applied Opt 39(6):897–912

Ruddick K.G, Cauwer V.D, Mol B.V (2005) Use of the near infrared similarity reflectance spectrum for the quality control of remote sensing data. SPIE 2005:#5585-1

Ruddick K.G, Cauwer V.D, Park Y.J (2006) Seaborne measurements of near infrared water-leaving reflectance: The similarity spectrum for turbid waters. Limnol Oceanogr 51(2):1167–1179

Shanmugam P, Ahn Y (2007) New atmospheric correction technique to retrieve the ocean colour from SeaWiFS imagery in complex coastal waters. J. Opt. A: Pure Appl. Opt. 9:511–530

Shettle E.P, Fenn R.W (1979) Models for the aerosols of the lower atmosphere and the effects of humidity variations on their optical properties. Env Res Papers 676:AFGL-TR-79-0214

Shi W, Wang M (2009) An assessment of the black ocean pixel assumption for MODIS SWIR bands. Remote Sens Environ 113:1587-1597

Siegel D.A, Wang M, Maritorena S, Robinson W (2000) Atmospheric correction of satellite ocean color imagery: the black pixel assumption. Aplied Opt 39(21):3582-3591

Spencer J.W (1971) Fourier Series Representation of the Position of the Sun. Search(2):172-177

Steinmetz F, Dechamps P.Y (2011). Atmospheric correction in presence of sun glint: application to MERIS. Optics Express 19(10):9783-9800

The Solar Spectral Irradiance from 200 to 2400 nm as Measured by the Solspec Spectrometer from the ATLAS and EURECA Missions. Solar Physics(214): 1–22

Wang M (1991) Atmospheric correction of the second generation ocean color sensors. Ph.D. dissertation (University of Miami, Coral Gables, Fla)

Wang M (2002) The Rayleigh lookup tables for the SeaWiFS data processing: Accounting for the effects of ocean surface roughness. Int J Remote Sens 23(13):2693–2702

Wang M (2002) Correction of artifacts in the SeaWiFS atmospheric correction: removing discontinuity in the derived products. Remote Sens Environ 84:603–611

Wang M (2005) A refinement for the Rayleigh radiance computation with variation of the atmospheric pressure. Int J Remote Sens 26(24):5651–5663

Wang M (2006) Effects of ocean surface reflectance variation with solar elevation on normalized water-leaving radiance. *Appl. Optics*, *45*(17),4122-4128

Wang, M. (2007), Remote sensing of the ocean contributions from ultraviolet to near-infrared using the shortwave infrared bands: simulations. *Appl. Optics*, *46*(9), 1535-1547.

Wang M, Shi W (2007) The NIR-SWIR combined atmospheric correction approach for MODIS ocean color data processing. Optics Exp 15(24):15722–15733

Wang M (2007) Remote sensing of the ocean contributions from ultraviolet to near-infrared using the shortwave infrared bands: simulations. Applied Opt 46(9):1535–1547

Wang M, Shi W, Jiang L (2012) Atmospheric correction using near-infrared bands for satellite ocean color data processing in the turbid western Pacific region. Opt Express 20(2):741-53

초록

본 논문은 세계최초의 정지궤도 해색 위성인 천리안 해색 위성 (GOCI : Geostationary Ocean Color Imager)의 데이터처리 소프트웨어 (GDPS : GOCI Data Processing System) 1.1 버전에 적용될 GOCI 의 표준 대기보정 알고리즘에 대해 기술하고 있다.

본 대기보정 이론은 대기입자간의 복수산란을 고려한 SeaWiFS 표준대기보정 방법에 이론적인 기반을 두고 있으며, case-2 탁수 보정, 에어로졸 모델 변경, 슬롯편차 개선 등 부분적인 보완이 추가적으로 이루어졌다.

본 연구는 특히 탁수 해역에서의 대기보정 개선에 초점을 맞추고 있는데, 근적외 파장대(NIR)에서 탁수해수반사도 추정을 위해 적색파장부터 근적외 파장영역까지의 해수 반사도 경험적 상관관계 모델을 4 차 다항식으로 구축하여 반복적인 계산을 통해 오차를 줄이는 방법을 적용하였다. 상관관계 모델링을 위한 해수 반사도 데이터는 탁수에 해당하는 픽셀에서 가장 인접한 맑은 해역의 대기보정 결과에서 얻어진 에어로졸 종류 및 광학두께 정보를 수평적으로 확장하여 다시 대기보정하고 여기에서 얻어진 해수 반사도 데이터들을 수집하였다. 이렇게 위성을 통해 수집된 NIR 파장대 해수 반사도 자료의 상관관계는 현장수집을 통해 얻어진 자료보다 더 좋은 상관관계를 보여주었다.

대기보정의 성능을 평가하기 위해서 본 연구에서는 2011 년 한 해 한반도 주변 해역 현장조사를 통해 수집한 정규수출광량 (nLw) 스펙트럼 자료와 비교검정 하였다. 대기보정의 검정결과, 탁도가 높은 해역에서 특히 좋은 성능을 보여주지만, 맑은 해역에서는 해수면 위 광측정 방법을 통해 발생하는 오차를 감안하더라도 아직 어느 정도 개선이 필요해 보인다. 이런 맑은 해역에서의 오차는 대기보정의 오차 뿐 아니라, 센서의 지상테스트 과정에서 발생하는 불확실성에 의해서도 발생한다. 추후

장기간 수집한 현장데이터 및 위성데이터를 통한 대리보정 (vicarious calibration) 등의 방법을 적용한다면 이 과정에서 발생하는 오차는 어느 정도 보완 될 수 있을 것으로 보인다.

주요어 : GOCI, 대기보정, 해색, case-2 해수, NIR 보정

감사의 글

지난 2 년동안의 대학원 생활을 마무리 하는 과정에서 뒤돌아 보면 새삼스럽게 많은 아쉬움이 남지만, 많은 분들의 도움과 따뜻한 관심 속에서의 질책들은 저를 또 다시 한 층 성숙해질 수 있는 계기를 마련해주었던 것 같습니다. 여러모로 부족한 졸업논문을 마치며, 많은 도움을 주신 분들께 이렇게 지면으로나마 감사의 인사를 남길 수 있어서 정말 다행인 것 같습니다.

우선 한없이 부족한 저를 올바르게 이끌어 주시고, 지금의 논문이 있기까지 학문적으로 인간적으로 아낌없는 가르침을 주신 오임상 교수님께 진심으로 감사 드립니다. 또, 해양광학 및 대기보정에 전혀 문외한이었던 저에게 아낌없는 가르침을 주시고 이끌어 주신 한국해양과학기술원의 박영제 박사님께도 감사의 마음을 전하고 싶습니다. 또, 저를 항상 신뢰하고 지원을 아끼지 않으셨던 한국해양과학기술원의 유주형 해양위성센터장님께도 진심으로 감사 드립니다. 덧붙여서 부족한 저를 위해 항상 아낌없는 조언을 주셨던 해양위성센터의 최종국박사님, 손영백 박사님, 이윤경 박사님께도 감사의 뜻을 전하고 싶습니다. 연구를 위해 바쁜 일정 속에서도 대량의 자료처리를 맡아서 고생하셨던 이순주 운영요원, 이보람 연구원, 그리고 위성센터 가족 여러분들에게도 감사 드리며, 특히 검정을 위한 모든 현장자료를 제공해주신 문정언 연구원님께도 진심으로 감사 드립니다. 대학원 생활 동안 동기들 이상으로 많이 응원해주고 힘이 되어준 동생들, 특히 정욱재, 박희망 그리고 극지연구소의 김윤정 연구원, 이승겸 연구원에게도 감사의 뜻을 전하고 싶습니다. 또, 멀리 떨어져 계심에도 불구하고 특별히 많은 관심과 조언을 아끼지 않으셨던 제게는 멘토 같으신 NOAA 의 손승현 박사님께도 꼭 감사의 말씀을 전해드리고 싶습니다.

마지막으로 항상 저를 믿고 응원해주며 마음 한구석에 언제나 든든하게 자리잡고 있는 수빈씨, 뒤늦은 나이에 학문에 뛰어들었음에도 불구하고 한결같은 사랑과

믿음으로 지켜봐 주시며 지원해주신 사랑하는 부모님들께 진심으로 감사 드리며 이 논문을 바칩니다.